FORTE Measurements of Global Lightning Altitudes

Michael Jay Peterson[1]

[1]ISR-2,Los Alamos National Laboratory
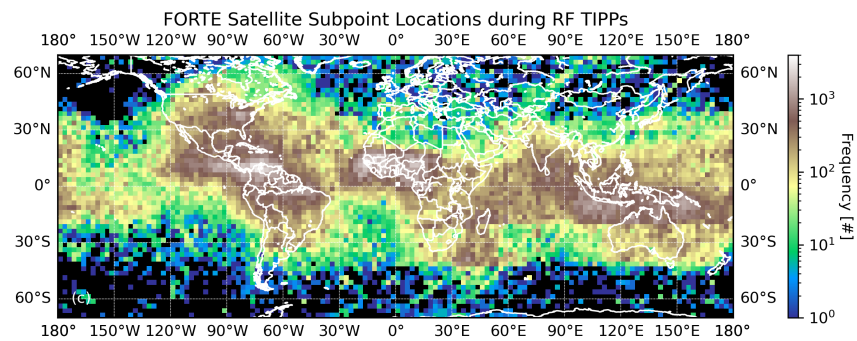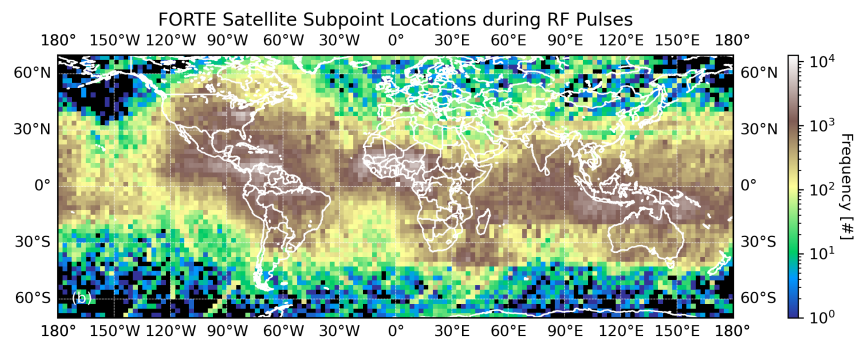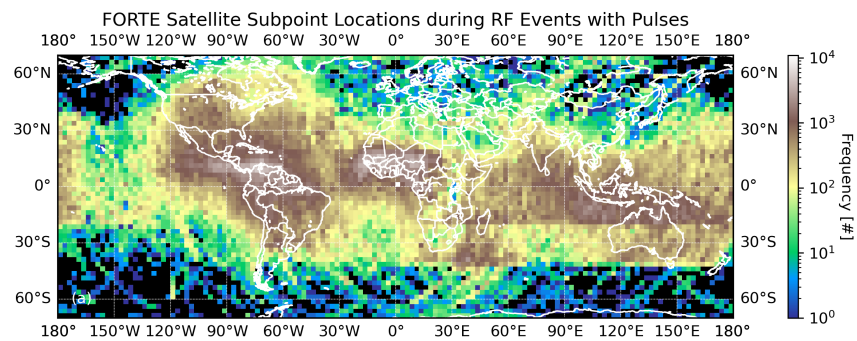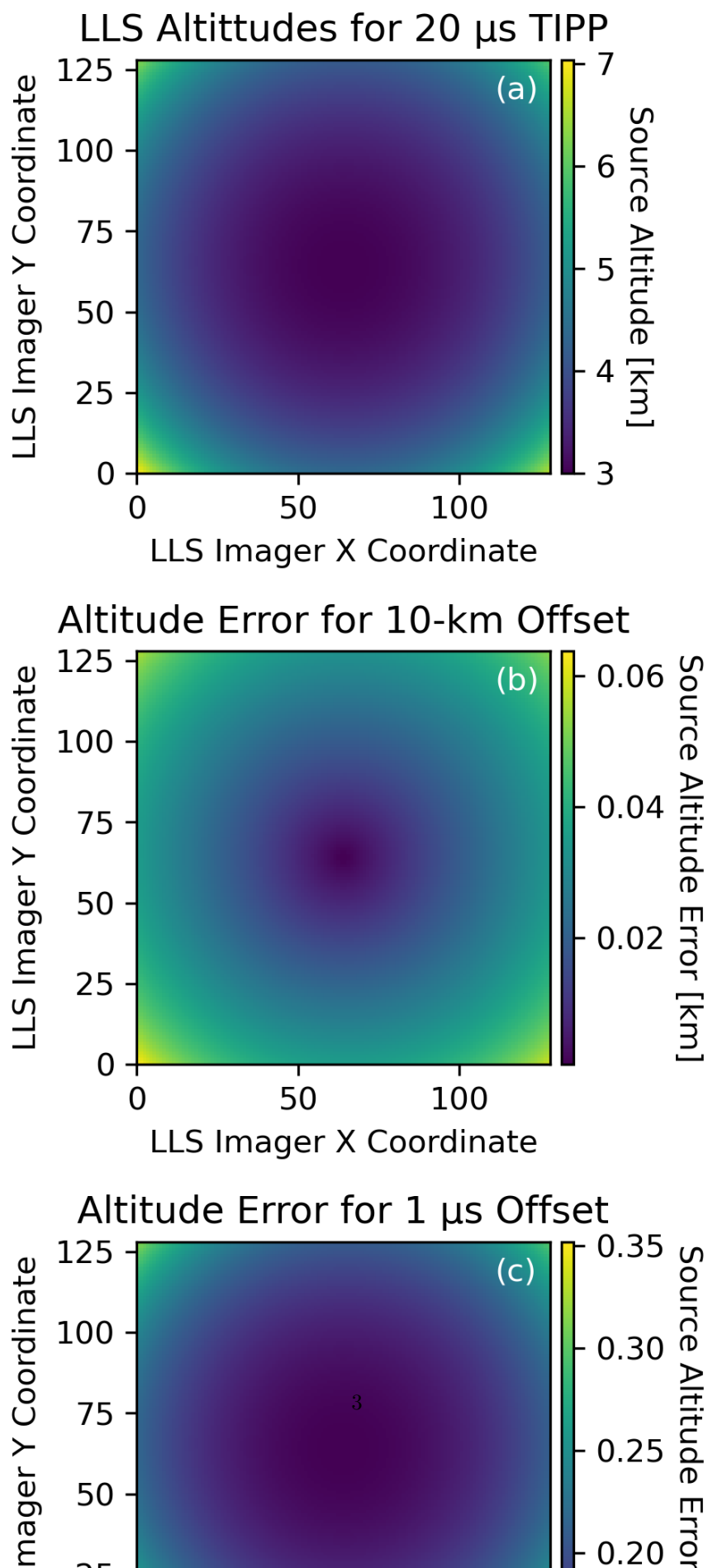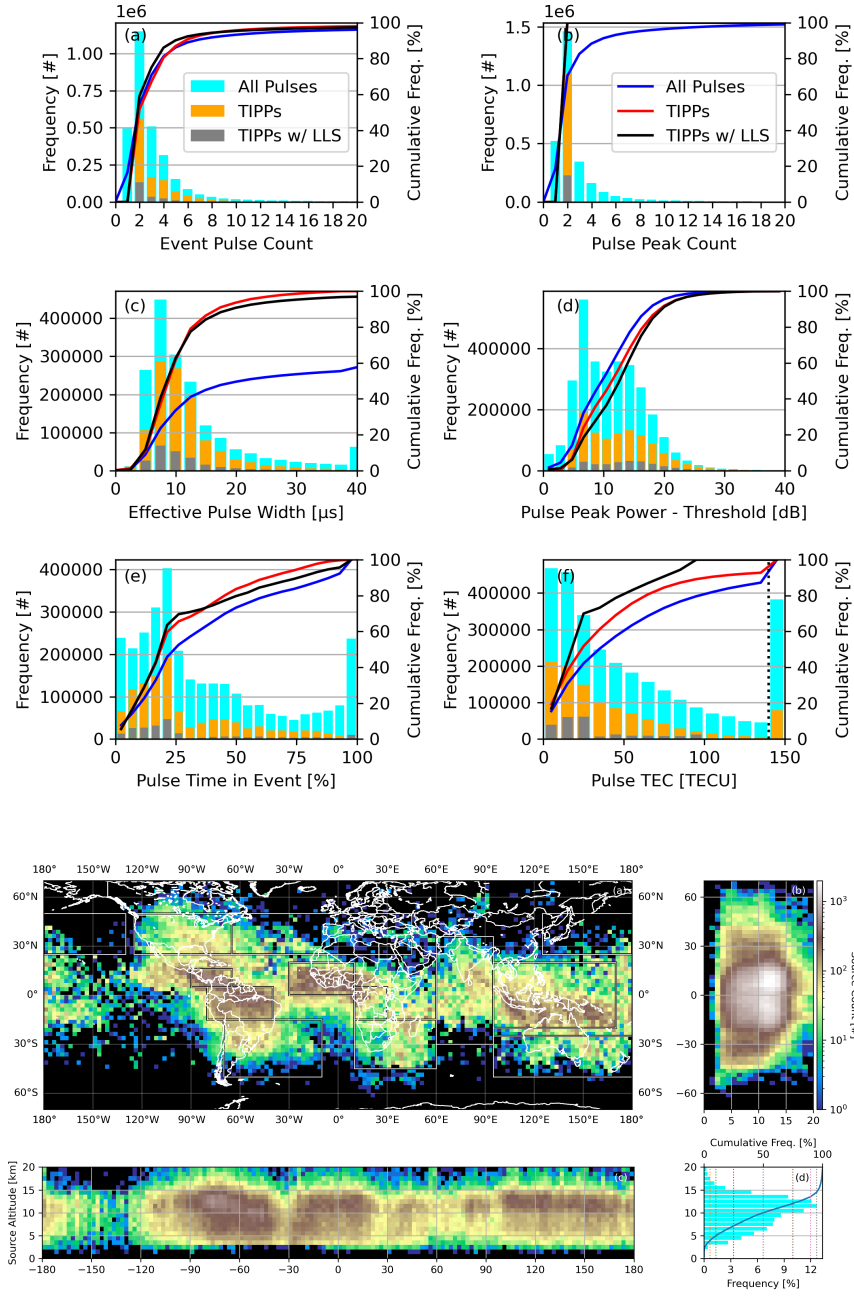
November 24, 2022

Abstract

While multiple lightning detection systems provide geographical locations of lightning events across the globe, robust lightning altitude measurements on a global scale have proven elusive. Space-based platforms have an advantageous viewing geometry over ground-based systems for making these measurements, but prior studies with the Fast On-orbit Recording of Transient Events (FORTE) satellite were limited to a few thousand events. In this study, we apply the same technique for calculating source altitude from the previous efforts to a large catalog of hundreds of thousands of global FORTE in-cloud lightning events that were coincident with flashes geolocated by its lightning imager between 1997 and 2003. We use this data to document global variations in lightning altitude. As in previous studies, we find that FORTE primarily resolves sources from the upper (positive) charge layer at ~11 km altitude in normal thunderstorms. However, sources are also recorded from other charge layers in the storm, and from leaders developing between layers. In particular, we note a pronounced increase in source altitude in the first 20 ms of FORTE flashes from the negative leader developing upward into the upper positive charge layer. Regions known for wintertime and/or stratiform lightning have increased contributions from low-altitude sources, while tropical regions particularly around Panama and the Maritime Continent have the greatest concentrations of high-altitude sources.

Hosted file

peterson-034-2022_forte_altitudes_si.docx available at https://authorea.com/users/530648/articles/602581-forte-measurements-of-global-lightning-altitudes

FORTE Satellite Subpoint Locations during RF Events with Pulses

FORTE Satellite Subpoint Locations during RF Pulses

FORTE Satellite Subpoint Locations during RF TIPPs

LLS Altittudes for 20 μs TIPP

(a)

LLS Imager Y Coordinate

LLS Imager X Coordinate

Source Altitude [km]

Altitude Error for 10-km Offset

(b)

LLS Imager Y Coordinate

LLS Imager X Coordinate

Source Altitude Error [km]

Altitude Error for 1 μs Offset

(c)

mager Y Coordinate

3

Source Altitude Error

1   **FORTE Measurements of Global Lightning Altitudes**

2

3   **Michael Peterson[1]**

4

5

6   [1]ISR-2, Los Alamos National Laboratory, Los Alamos, New Mexico

7

8

9

10

11

12   Corresponding author: Michael Peterson (mpeterson@lanl.gov), B241, P.O. Box 1663 Los
13   Alamos, NM, 87545

14

15

16   **Key Points:**

17   - A joint RF / optical method for retrieving lightning altitude from previous studies has
18   been applied to the full FORTE record

19   - While global FORTE events concentrate in the upper (positive) charge layer at ~10 km,
20   sources are also found at lower altitudes

21   - Source altitude is shown to depend on location, land or ocean terrain, season, and time in
22   the parent flash

23   **Abstract**

24   While multiple lightning detection systems provide geographical locations of lightning

25   events across the globe, robust lightning altitude measurements on a global scale have proven

26   elusive. Space-based platforms have an advantageous viewing geometry over ground-based

27   systems for making these measurements, but prior studies with the Fast On-orbit Recording of

28   Transient Events (FORTE) satellite were limited to a few thousand events. In this study, we

29   apply the same technique for calculating source altitude from the previous efforts to a large

30   catalog of hundreds of thousands of global FORTE in-cloud lightning events that were

31   coincident with flashes geolocated by its lightning imager between 1997 and 2003. We use this

32   data to document global variations in lightning altitude.

33   As in previous studies, we find that FORTE primarily resolves sources from the upper

34   (positive) charge layer at ~11 km altitude in normal thunderstorms. However, sources are also

35   recorded from other charge layers in the storm, and from leaders developing between layers. In

36   particular, we note a pronounced increase in source altitude in the first 20 ms of FORTE flashes

37   from the negative leader developing upward into the upper positive charge layer. Regions known

38   for wintertime and/or stratiform lightning have increased contributions from low-altitude

39   sources, while tropical regions particularly around Panama and the Maritime Continent have the

40   greatest concentrations of high-altitude sources.

41

42   **Plain Language Summary**

43   After many years of observing lightning from by multiple sensors, we have a good

44   understanding of where lightning occurs in the world and how its frequency differs from region

45   to region. However, the lightning that we witness on the ground (which is also the primary

46   phenomenon detected by the global lightning networks) is only a small portion of the expansive

47   lightning channels. Most of the flash extends through the clouds, hidden from view. The altitudes

48   of lightning flashes in the clouds are particularly important because they reveal changes to

49   convection and play a key role in atmospheric chemistry. In this study, we use a large global

50   catalog of in-cloud lightning events recorded by the FORTE satellite to document lightning

51   altitudes across the globe.

52

1 Introduction

53

54   The altitude of lightning within the cloud is controlled by the kinematics of the parent

55 thunderstorm that organize charged precipitation particles into spatially-separated pockets with a

56 surplus of either positive or negative charge. Under typical conditions in the Non-Inductive

57 Charging (NIC) mechanism (Reynolds et al., 1957; Takahashi, 1978; Jayaratne et al., 1983;

58 Saunders et a.l, 1991; Saunders & Peck, 1998; Takahashi & Miyawaki, 2002; Mansell et al.,

59 2005), collisions between graupel rimed with supercooled liquid water and small ice particles in

60 the thunderstorm updraft result in the heavier graupel attaining a negative charge and the lighter

61 ice particles becoming positively charged. The updraft sorts these species of hydrometeors by

62 mass, lofting the positively-charged ice particles towards the top of the cloud, while leaving the

63 negatively-charged graupel in the mid-levels of the storm. This creates the main positive dipole

64 (Wilson, 1920) that we see in the tripole structure of ordinary thunderstorms (Simpson and

65 Scrase, 1937; summarized in Williams, 1989).

66   However, the diversity and complexity of thunderstorms leads to many different charge

67 structures being observed that diverge substantially from this idealized tripole view. Some

68 storms conflict with the tripole model entirely (i.e., Marshall and Rust, 1991), while others

69 consist of a convective core with a primarily tripole structure adjacent to non-convective

70 electrified clouds with their own unique charge structures. One notable example of a non-

71 convective cloud with a distinct charge structure is the electrified anvil cloud. The upper positive

72 layer extends laterally beyond the edge of the convective core into the overhanging anvil, and

73 negative screening layers form on the upper and lower boundaries of the anvil cloud (Marshall et

74 al., 1989). Additionally, electrified stratiform clouds are comprised of multiple vertically-

75 confined yet horizontally-extensive layers of alternating positive and negative charge created by

76   in-situ electrification processes and the advection of charge from the convective core (Stolzeburg

77   et al., 1998; Schuur and Rutledge, 2000; Ely et al., 2008; Lang and Rutledge, 2008).

78   Thunderstorm charge structures also vary by season and location on Earth (summarized in

79   Williams, 2018), with the inner tropics having particularly tall thunderstorms (López et al., 2019)

80   and winter thunderstorms over the oceans surrounding Japan being well-known for their compact

81   vertical extent (Yamamoto et al., 2006).

82   Because lightning flashes consist of positive and negative leaders that develop through

83   these charge regions, it is possible to infer the charge structure of a given thunderstorm from the

84   altitudes of lightning emissions sources. The key advantage of this approach over in-situ balloon

85   soundings is that lightning source altitudes can be measured remotely at considerable distances

86   using Radio-Frequency (RF) measurements. Lightning Mapping Arrays (LMAs: Rison et al.,

87   1999) are networks of Very High Frequency (VHF) band RF receivers that are capable of

88   mapping the three-dimensional structure of lightning flashes with a nominal accuracy of tens of

89   meters (Thomas et al., 2004) and a maximum range on the order of a few hundred kilometers

90   (depending on the number of stations in the array and their geometry). The locations of

91   individual charge layers manifest as local maxima in the VHF source altitude profile, while the

92   polarity of each layer can be inferred from the relative frequency of sources (Rison et al., 1999).

93   This is possible because lightning processes associated with a negative leader propagating

94   through a positive charge layer are more prevalent emitters of VHF radiation than positive

95   leaders propagating through a negative charge layer. Manual techniques and, more recently,

96   automated routines like chargepol (Medina et al., 2021), use VHF source altitudes to characterize

97   the bulk thunderstorm charge structure.

98   In addition to informing thunderstorm charge structures, lightning altitude measurements

99   are also useful for revealing changes in updraft behavior (Suszcynsky and Heavner, 2003; Fierro

100   et al., 2011) and quantifying the effects of lightning on atmospheric chemistry. Nitrogen oxides

101   ($NO_x = NO+NO_2$) are a catalytic precursor in the photochemical production of tropospheric

102   Ozone (O_3) (Crutzen, 1973; Chameides and Walker, 1973; Seiler and Crutzen, 1980; Crutzen et

103   al., 1979), which is an important greenhouse gas in the upper troposphere (Fishman et al., 1979;

104   Lacis e al., 1990). Numerous sources contribute to the NO_X budget including ground-level

105   sources such as biomass and hydrocarbon burning, and atmospheric sources including aircraft

106   emissions and lightning (LNO_x). Ivanov et al. (2014) identified the temperature threshold for

107   NO_x production to occur as 3000-4000 K. The lightning leaders that can be mapped with VHF

108   measurements like LMAs typically have temperatures around 10,000 K (Rakov et al., 2003).

109   Thus, these leaders are an important source of LNO_x, and the LNO_x output from individual

110   flashes is expected to be concentrated at the altitudes where the leaders propagate. Multiple

111   lightning altitude profiles have been created from either lightning measurements or

112   parameterizations that can be used to estimate the LNO_x mass distribution for regional and global

113   chemical transport models (Pickering et al., 1998; DeCaria et al., 2000; Tie et al., 2002; Labrador

114   et al., 2005; Luo et al., 2017; Carey et al., 2016; Mecikalski and Carey, 2018). However, none of

115   these profiles are representative of global lightning. The parameterizations rely on many

116   assumptions about how lightning altitude scales with environmental parameters, while the

117   measured profiles were created from regional 3D lightning mapping systems (LMAs and others)

118   that have limited ranges and only cover certain land-based regions of the Earth (which are

119   heavily concentrated in the northern mid-latitudes).

120   Altitude profiles of VHF lightning sources are also available from space-based RF

121   measurements. Jacobson et al. (1999) described a methodology for using the time delay between

122 the VHF pulses produced by the direct line-of-sight measurement of an in-cloud lightning source

123 and its reflection off the surface of the Earth to compute the altitude of the source above ground

124 level. This method requires that the position of the satellite and the geographic location of the

125 source be known. Light and Jacobson (2002) used this approach to generate VHF source altitude

126 distributions for FORTE events coincident with either the National Lightning Detection Network

127 (NLDN: Cummins et al., 1998) or FORTE's Optical Lightning System (Suszcynsky et al., 2001).

128 The advantage of using FORTE satellite observations is that its Low Earth Orbit (LEO) vantage

129 point is not subject to the regional biases of LMAs. However, Light and Jacobson (2002) only

130 had a small sample on the order of 1000 coincident lightning events available, which was not

131 sufficient to examine variations in lightning altitude across the globe.

132   In this study, we apply the same approach as Jacobson et al. (1999) and Light and

133 Jacobson (2002) to our comprehensive catalog of joint RF-optical FORTE detections to produce

134 document the lightning altitudes across the globe. This initial overview of our new global

135 lightning altitude dataset will focus on regional and seasonal variations in the source altitude

136 distribution, and the altitudes of lightning flashes. Future work will explore other applications of

137 the FORTE lightning altitude data.

138

139 **2 Data and Methodology**

140   2.1 The FORTE Satellite

141   The FORTE satellite was launched into a nearly circular orbit with a 70º inclination and

142 825 km altitude in August 1997. It recorded both optical and VHF lightning events from 1997

143 until 2003, and optical-only events until 2010. FORTE was unique not only for providing both

144   optical and RF lightning measurements of lightning from the same apace-based platform, but

145   also for being operated in a variety of modes while on-orbit. The FORTE instruments could be

146   commanded to operate autonomously or have one instrument trigger another, the record lengths

147   and threshold settings could be changed while on-orbit, or individual instruments could be turned

148   off to conserve on-board memory for the remaining sensors. As a result, the FORTE dataset is

149   heterogeneous, and only a small fraction of the lightning events observed by FORTE have

150   coincident detections from the FORTE RF system as well as both sensors that comprise the

151   FORTE Optical Lightning System (OLS). These instruments and their operating modes are

152   described below.

153   2.1.1 The FORTE Lightning Location System

154   The first OLS instrument that we will discuss is the FORTE Lightning Location System

155   (LLS) (Suszcynsky et al., 2000). The LLS was a pixelated lightning imager whose role was to

156   geolocate lightning events to within a nominal pixel (~ 10 km) over its 80° FOV. It was built

157   from modified hardware from NASA's Lightning Imaging Sensor (LIS: Christian et al., 2000),

158   with a front-end optical assembly and Charge Coupled Device (CCD) imaging array identical to

159   LIS and an operations and signal processing module designed by Sandia National Laboratories.

160   Like LIS, the LLS operated autonomously and triggered whenever the signal amplitude

161   in one of the pixels on its 128x128 imaging array during one of its 2.47 ms integrating frames

162   exceeded a threshold above the background value. However, unlike LIS, flash clustering and

163   background characterization was not performed, and thus could not inform the LLS signal

164   processing. As a result, the LLS could not take advantage of cluster-based energetic particle and

165   glint filters like the LIS filters described in Christian et al. (2000). The SNL signal processing

166   module did not screen for energetic particles, and the FORTE operators, instead, elected to turn

167   the LLS off during certain orbits that took FORTE through the South Atlantic Anomaly.

168   Moreover, a very simple and severely-limiting glint filter was implemented where individual

169   LLS pixels would be turned off once they were illuminated for three-or-more consecutive

170   frames. As a result, long-lasting lightning processes like Continuing Current (Bitzer, 2017) were

171   not as well captured by the LLS as they were with LIS.

172   Since flash clustering was not performed during the FORTE mission, we constructed

173   cluster feature data for the LLS in Peterson et al. (2021a,b). We first converted the LLS

174   detections that were termed "events" in the LLS literature (Suszcynsky et al., 2000), but were

175   more akin to LIS series features (Peterson and Rudlosky, 2019), into the single-pixel, single-

176   frame features that are termed events in the LIS literature (Christian et al., 2000; Mach et al.,

177   2007). Next, we clustered these extracted events into "groups" describing contiguous regions of

178   cloud illumination in a single integration frame, "series" that describe periods of sustained

179   illumination over time, flashes that approximate distinct lightning flashes, and "areas" that

180   approximate individual thunderstorms.

181   2.1.2 The FORTE Photodiode Detector

182   The second instrument in the OLS payload was the FORTE photodiode detector (PDD).

183   The PDD measured broadband (0.4 μm – 1.1 μm) optical waveforms from lightning events over

184   its 80° circular Field of View (FOV), which covered a ~1200 km footprint on the surface of the

185   Earth (Kirkland et al., 2001; Suszcynsky et al., 2000). The PDD had a sampling interval of 15

186   microseconds and a variable record length. Under autonomous triggering, PDD records captured

187   1.92 ms of data, while external triggers produces 6.75 ms records.

188   The PDD rejected false events from energetic particle impacts by requiring that the PDD

189   signal exceed the background threshold over a specified number of samples ranging from 0 (off)

190   to 32. However, a typical value during the FORTE mission was 5, equating to 75 microseconds.

191   The PDD was also subject to trigger rate limitations including a minimum dead time

192   approximately equal to the record length between successive triggers, and a configurable limit on

193   the maximum number of triggers allowed over a short time interval. Once this latter limit was

194   reached, the PDD would stop triggering until it received the next GPS-derived 1-Hz signal

195   (Kirkland et al., 2001). While nominally employed to mitigate glint artifacts, this limit also

196   prevented the FORTE PDD from capturing later activity in lightning flashes.

197   As with the LLS, we constructed cluster feature data for the PDD in Peterson et al.

198   (2021a,b). However, the exceptional temporal sampling of the PDD allowed us to expand the

199   data tree to finer scales by defining smaller-scale features than the typically ~2 ms events. The

200   basic unit of PDD clustering becomes the 15-microsecond "sample" feature, which cluster into

201   "pulses" that will be described in Section 2.2.

202   2..1.3 The FORTE RF System

203   The FORTE RF system consisted of two different types of broadband VHF receivers: the

204   Two And Twenty Receiver" (TATR) and the "HUndred Megahertz Receiver" (HUMR). These

205   receivers were connected to FORTE's two identical Log-Periodic Antennas (LPAs) that were

206   mounted orthogonal to each other along the nadir-pointing boom (Jacobson et al., 1999;

207   Suszcynsky et al., 2000; Shao and Jacobson, 2001; Light et al., 2001b). TATR and HUMR

208 recorded VHF waveforms from global lightning from late 1997 until 2003 across a 20 – 300

209 MHz band.

210   The TATR payload consisted of two receivers (TATR-A and TATR-B) that would each

211 sample one of the FORTE LPA antennas. Each receiver could be independently tuned, and

212 would provide VHF measurements across a 22-MHz subband. In addition to tuning, TATR

213 record lengths and the ratios of pre-trigger to post-trigger samples were also reconfigured

214 throughout the FORTE mission, providing a heterogenous collection of VHF measurements from

215 global lightning events. The HUMR payload consisted of a single receiver that sampled a wider

216 85 MHz band. As with TATR, HUMR could be tuned to different frequencies across the VHF

217 spectrum. However, HUMR records were also generally longer than TATR records. The longer

218 6.75 ms PDD records mentioned previously were coincident with HUMR records of a

219 comparable length.

220   The FORTE RF system had multiple triggering modes including a manual trigger mode

221 for on-orbit testing, an external trigger mode to capture RF waveforms from OLS events, and an

222 autonomous trigger mode. These different modes are summarized in Light (2020). The

223 autonomous trigger mode leveraged the wideband nature of lightning pulses to screen for

224 terrestrial noise, which tends to be comprised of narrowband carrier signals. The wideband RF

225 signal was divided into eight evenly-space 1-MHz channels across the receiver passband. RF

226 power was monitored in each of these channels, and an "alarm" was issued whenever the power

227   in one of the channels exceeded a noise-riding threshold. If multiple channels (usually 5)

228   produced simultaneous alarms, the RF system would trigger and report an event.

229   RF events and their waveform records are also clustered into features like the PDD and

230   LLS data. The RF "sample" and "pulse" features will be described in the next section. Finally,

231   all of the cluster features from each of the three FORTE instruments are cross-linked to facilitate

232   comparisons between sensors.

233   2.2 Signal Processing and Pulse Extraction

234   Both the PDD and RF system provide waveform data for each recorded event that might

235   contain one or more distinct pulses from various lightning phenomena. In the original clustering

236   described in Peterson et al. (2021a), we identified pulses as features bounding contiguous

237   samples that exceeded the background value by a specified threshold. This approach was applied

238   directly to the PDD irradiance data, and to the RF data after signal processing. The RF

239   waveforms were first "prewhitened" to remove manmade carrier waves from the wideband

240   measurements and then "dechirped" to counteract the frequency-dependent delay in the signal

241   time of arrival from propagation through the ionosphere. These standard procedures in FORTE

242   studies are described in Light (2020). Pulses were then identified in the timeseries of average

243   power across the band. For the TATR data, where we have 2 independent waveforms from each

244   event, we use only the waveform that has the greatest signal amplitude to extract pules.

245   While this approach is sufficient for simple PDD and RF waveforms dominated by

246   discrete high-amplitude pulses, it is not well-suited for distinguishing pulses in complex

247   waveforms that contain multiple pulses of varying amplitude, spacing, and effective width.

248   Therefore, we developed new approach that could be applied to either the PDD or RF data to

249 extract and characterize pulses over a variety of waveform shapes. Pulses and their child "peak"

250 features are found by looping from the maximum signal amplitude down to the noise threshold.

251 A new pulse feature is created when samples are found that both exceed the incremental

252 threshold and do not occur within a specified time threshold of an existing pulse. If a new pulse

253 is not identified, the existing pulses are expanded to include the new samples that exceed the

254 incremental threshold. This new approach permits a single contiguous portion of the waveform

255 that contains multiple prominent peaks separated in time to be partitioned into two or more pulse

256 features. The old approach would always identify a single pulse feature in these complex

257 waveforms.

258   To demonstrate pulse extraction, Figure 1 shows an example dechirped TATR waveform

259 that contained two Trans-Ionospheric Pulse Pairs (TIPPs) from in-cloud lightning events and a

260 third solitary pulse. The band-averaged power timeseries (solid black line) is first smoothed

261 (solid red line), and the pulse feature threshold is determined as 3x the standard deviation above

262 the minimum value in the smoothed curve (top dashed horizontal line). The iterative threshold

263 method described above identifies 5 peak features (solid blue lines) in 5 pulse features (blue bars

264 in Figure 1b with dashed vertical lines indicating their endpoints). Pulse characteristics are then

265 computed using windows that encapsulate the pulse plus a 20 microsecond buffer on either side

266 (grey boxes in Figure 1b). Finally, TIPPs are identified as impulsive features that are in close

267 temporal proximity to another impulsive feature. The constituent pulses in each TIPP are then

268 linked (solid horizontal black lines in Figure 1b), and the peak-to-peak time difference for the

269 TIPP is recorded.

270   In TIPP cases where multiple candidate links might be made (as with pulses 3 and 4 in

271 Figure 1b), feature links are prioritized by minimizing a Weighted Euclidean Distance (WED)

272   function of the differences in time and feature attributes (i.e., pulse width, peak power, rise time,

273   etc.). In Figure 1b, Pulse 3 was linked to Pulse 4 because it produced the lowest WED values of

274   the remaining features, even though Pulse 4 was a better match for Pulse 5. A common cause of

275   these differing links is that only one of the pulses in the TIPP exceeded the noise threshold,

276   which appears to be the case here. To mitigate this potential source of uncertainty in the pulse

277   separation times, we only consider TIPPs where both constituent pulses identify the other as its

278   partner, as with Pulse 4 and Pulse 5. The two pulses that comprise each linked TIPP are

279   integrated into a single entry in our feature database.

280   Applying these methods to all types of RF events in the FORTE record produces the

281   pulse statistics shown in Figure 2. Events whose power timeseries were too flat to produce any

282   pulse features are not considered. Most of the remaining events contain only 1 or 2 pulses

283   (Figure 2a) – with a peak at 2 due to the prevalence of TIPPs in the data. However, the remaining

284   40-50% events (depending on the category) contain more than 2 pulses. These may be trains of

285   weak TIPPs from in-cloud events, a Cloud-to-Ground (CG) stoke with a TIPP, or a diffuse in-

286   cloud event (i.e., a K-change) with embedded impulsive in-cloud events. The longer events in the

287   FORTE RF record that last multiple milliseconds can contain dozens of distinct pulses. The

288   number of individual peaks in a given pulse (Figure 1b) also varies by pulse type. Nominally,

289   each pulse will have a single peak per pulse (or 2 peaks per TIPP). However, 17% of pulses have

290   3-or-more peaks. Analyzing these events (not shown for brevity) indicates that they tend to be

291   mixed events where the peaks (including TIPPs) were not sufficiently isolated in time from the

292   other nearby peaks to create separate pulse features.

293   Pulse features also have a wide range of effective widths (Figure 2c). The median

294   effective width for an individual pulse in a TIPP is 8 microseconds, and the prevalence of TIPPs

295   in the FORTE data heavily biases the general pulse width statistics. Only ~40% of general pulses

296   in our database have effective widths exceeding 40 microseconds, with the peak at 40

297   microseconds being artificial due to the thresholds used in the algorithm. These thresholds also

298   control the minimum signal amplitude that results in a pulse being identified (Figure 2d). Few

299   general pulses and hardly any TIPPs are resolved with a peak amplitude < 2 dB above the noise

300   threshold. Most pulses exceed the threshold by at least 5 dB. Pulses like Pulse 1 and 2 in Figure

301   1b are more common in our dataset than Pulses 4 and 5 because the threshold is set fairly high

302   compared to the actual noise floor in order to reduce the number of spurious events. This also

303   means that, while we do not restrict our sample to lowband (20-50 MHz) TATR detections, these

304   events dominate because lightning is more powerful in the lowband and the HUMR waveforms

305   tend to be noisier than TATR waveforms.

306   These pulses also occurred throughout the RF event record (Figure 2e). The most

307   common location in the record was around 25% of the record length, with increased frequencies

308   earlier in the record compared to later. This is due to both the commanded pretrigger fraction and

309   the dechirping process pushing the signal back to its vacuum time of arrival. Higher TEC values

310   will result in larger temporal displacements than lower TECs. This can pose a problem for

311   characterizing pulses at the beginning of the RF record. The initial portion of a broader pulse or

312   the first constituent pulse of an early TIPP can be rolled around to the end of the record by the

313   dechirping algorithm. This is why there is a second peak in Figure 2e at the end of the record. It

314   is not physical, but rather an artifact of dechirping.

315   Pulses traversing the ionosphere along paths with high TEC values were observed by

316   FORTE due to its global observation domain and large effective FOV (Figure 2f). Our identified

317   pulses were subject to TEC values ranging from near 0 TECU to greater than 120 TECU (Figure

318   2f). Moreover, the dechirp algorithm failed in certain events, while there were other events that

319   resulted from onboard discharges on the spacecraft . Both of these scenarios yield a reported

320   TEC ≤ 0 TECU, and are shown in the rightmost bin in Figure 2f.

321   2.3 Filtering LLS-Coincident RF Events

322   The pulse statistics in Figure 2 indicate that we can use automated routines to create a

323   robust sample of distinct RF pulses from the FORTE data. However, these pulses need to be

324   filtered to ensure that the VHF source altitudes are physically meaningful. Pulses that lack LLS

325   coincidence will not be useful. Meanwhile, pulses that occur at the beginnings or ends of the

326   record, or that report a TEC ≤ 0 TECU will yield questionable pulse time differences.

327   However, the FORTE sampling of global pulses is already uneven – due in large part to

328   the heterogeneous FORTE commanding – and filtering the RF data further impacts the global

329   distribution of detected VHF sources. Table 1 summarizes the pulse counts in our global sample.

330   In total, 3 million distinct pulses are identified including 1 million TIPPs (36% of all pulses).

331   Figure 4 shows global distributions of RF events with pulse features (Figure 4a), all RF pulse

332   features (Figure 4b), and RF TIPPs (Figure 4c) according to the FORTE satellite subpoint. While

333   FORTE detections of the pulses in Table 1 are generally concentrated in the tropics, and

334   particularly around the tropical landmasses of the Americas, Africa, and the Maritime Continent,

335   all three global source distributions differ substantially from lightning climatologies derived

336   from NASA sensors (Cecil et al., 2014; Albrecht et al., 2016; Peterson et al., 2021c). Perhaps the

337   most notable departures occur in Africa, where VHF sources are prevalent in west Africa while

338   being infrequent in the primary lightning hotspot of the Congo Basin. Additionally, horizontal

339   striping can be noted in the Indian Ocean and Asia where RF detections are concentrated within

340   a latitude band surrounding the equator. A second band is also apparent in the Southern Ocean.

341   LLS coincidence is required to compute source altitude, but this requirement convolutes

342   the sampling biases from the two sensors. To minimize these biases to the extent possible while

343   preserving a reasonable sample size, we elect to take a "flash-level" approach to defining LLS

344   coincidence. We treat the RF event as an "event" feature in the LLS clustering scheme, which is

345   based on LIS clustering in Christian et al. (2001). All LLS events that occur within 330 ms of the

346   RF pulse are assumed to be candidates for the location of its origin. We compute this location as

347   the radiance-weighted mean position of all events that occur in the prescribed time window.

348   Under normal circumstances, all of these events would come from the same parent flash, or at

349   least the same parent thunderstorm area, and the RF source would be geolocated to a point within

350   10-30 kilometers of its true location. However, it is possible to have multiple ongoing

351   thunderstorms producing events within the LLS FOV at the same time. When this occurs, the RF

352   source location is weighted towards the more active thunderstorm.

353   Of the original 1 million RF TIPPs, the flash-level LLS coincidence requirement limits

354   the sample size to 380,000. These are the "TIPPs with LLS" entries in Figure 2. These LLS-

355   coincident TIPPs have similar effective width statistics to normal TIPPs (Figure 2c), are

356   somewhat more powerful (Figure 2d), and their times similarly peak at 25% of the record length

357   (Figure 2e), indicating that they were commonly the triggering pulse. However, their slant TECs

358   in Figure 2f are significantly lower than the 20-30 TECU medians for the other pulse categories.

359   This is due to two known biases imposed by the LLS: (1) the smaller 80° LLS FOV removed

360   events that originate near the limb and traverse nearly horizontally through the ionosphere

361   (experiencing high TECs) from the sample and (2) the LLS being more capable of detecting

362   lightning at night (when TECs are low) compared to during the day (when TECs are high).

363   Diurnal performance differences were also an issue with LIS that had to be compensated for

364   when creating the global lightning flash rate climatologies (Cecil et al., 2014; Albrecht et al.,

365   2016; Peterson et al., 2021c).

366   If we exclude pulses that have invalid TECs or that occur in the first or last 5% of the

367   record, we are left with 2.4 million events, 907,083 of which (37%) are TIPPs. Of these TIPPs,

368   300,214 have LLS coincidence at the flash level. Finally, if we further exclude pulses that occur

369   within 100 microseconds of another pulse (like Pulse 3 in Figure 1), the sample size is reduced to

370   1.8 million pulses and nearly 695,146 TIPPs (39%), 202,062 of which have LLS coincidence.

371   We can also optionally require that only a single LLS flash or LLS area is active at the time of

372   the RF event. This further reduces the sample to 152,995 LLS-coincident TIPPs at the area level

373   and 130,261 LLS-coincident TIPPs at the flash level. This filtering leaves us with 100k - 200k

374   TIPPs from across the globe that we can use to compute the VHF source altitudes, a sample that

375   is two orders of magnitude larger than Light and Jacobson (2002).

376   2.4 Calculating the Altitudes of Global VHF Sources

377   Jacobson et al. (1999) derived the following equation for the altitude of the VHF source

378   responsible for a TIPP:

379
$$a = c \cdot \tau \frac{\sin \beta}{1 - \cos 2\beta}$$

380   where c is the speed of light, τ is the time delay between the pulses that comprise the TIPP, and

381   β is the satellite elevation angle, which can be computed from the satellite position and the

382   latitude and longitude of the source. This equation assumes a spherical Earth where the source is

383   close to the surface.

384   Our use of flash-level LLS coincidence to geolocate the source is only justified as long as

385   the locations errors geolocating to the wrong part of the storm or flash (i.e., a few tens of

386   kilometers) only result in small altitude errors. To test this, we compute the altitude of a TIPP

387   with a 20 microsecond pulse separation at each point across the LLS FOV in Figure 4a, and then

388   the altitude error that would result from the TIPP being offset 10 km radially outward from its

389   true position in Figure 4b. Within the limited 80° LLS FOV, the maximum error in altitude for

390   being displaced by 10 km is only expected to be around 60 m. Therefore, we can be off by even a

391   few tens of kilometers without observing a notable effect on the altitude statistics.

392   The key parameter to measure precisely is the time difference between the two peaks in

393   the TIPP. Figure 4c computes the altitude error from being off by just 1 microsecond for a source

394   at each point on the LLS imaging array. Each microsecond of error results in an altitude error of

395   between 150 m at nadir to 350 m at the edge of the LLS FOV. It only takes a 3 microsecond

396   error for an edge source to be displaced in altitude by a full kilometer.

397

398   **3 Results**

399   The following sections will document the FORTE distributions of lightning altitudes

400   derived from LLS-coincident VHF source data. Section 3.1 will examine global distributions of

401   VHF source altitude. Section 3.2 will consider variations in the lightning altitude distributions

402   between different regions of the Earth and between each season. Section 3.3 will examine the

403   VHF source altitude distributions from LLS flashes.

404   3.1 Global Distributions of VHF Lightning Source Altitude

405   The FORTE orbit covered all of the major lightning-producing regions of the Earth, but

406   these regions were not sampled consistently, as we saw in the global distributions of RF events

407   and pulses in Figure 3. Requiring LLS coincidence substantially reduces the sample of events,

408   which can be noted in Table 1. The global distribution of LLS-coincident RF TIPPs is shown in

409   Figure 5. Figure 5a is analogous to the plots from Figure 3, except the FORTE satellite subpoint

410   position is replaced with the geolocated LLS position. The same RF event hotspots in the

411   Americas, west Africa, and the Maritime Continent can be noted, but the LLS coincidence

412   requirement removes the horizontal banding in the distribution while limiting the number of

413   samples at mid to high latitudes (particularly over the Eurasian continent).

414   Source altitude distributions by latitude (Figure 5b) and longitude (Figure 5c) are shown

415   to the right of and below the global distribution in Figure 5a, while the global altitude profile is

416   plotted in Figure 5d. Source altitudes are dominated by the upper charge layer at 10-12 km

417   altitude, which is normally positively charged and where negative leaders that are good emitters

418   of VHF radiation propagate. Light and Jacobson (2002) also identified peaks in their VHF

419   emitter altitude profiles in this range. Lower-altitude sources are less frequent and are usually

420   found between 5 km and 10 km.

421   However, not all regions conform to the global profile in Figure 5c, and some regional

422   differences can even be noted in the overall latitude (Figure 5b) and longitude (Figure 5c)

423   distributions. Low-altitude sources are more common over the longitude range associated with

424   the Americas chimney region compared to the Maritime Continent chimney region. While the

425   Africa chimney in the Congo Basin is not well resolved, the west Africa maximum has a greater

426   proportion of low-altitude sources along the west African coast compared to in the east over the

427   continent. The source distributions also tend to be taller at low latitudes near the equator in

428   Figure 5b compared to the mid-latitudes where, a subtle low-altitude peak at 6 km altitude is

429   faintly visible.

430   3.2 Regional and Seasonal Variations in Lightning Altitude

431   Due to the uneven sampling of the data, we will focus our discussion around altitude

432   profiles that have first been normalized by the local event count (i.e., Figure 5d). Twelve global

433   regions are boxed in Figure 5a that roughly correspond to the northern hemisphere mid-latitudes,

434   the northern hemisphere tropics, the southern hemisphere tropics, and the southern hemisphere

435   mid-latitudes for the three continental chimneys: the Americas, Europe and Africa, and Asia. The

436   VHF source altitude profiles for each of these regions are shown in Figure 6 organized

437   horizontally by longitude and vertically by latitude.

438   The source altitude distributions in these regions differ from the global altitude profile in

439   Figure 5d. The continental United States (Figure 6a) has a pronounced plateau between 5 km and

440   10 km similar to the NLDN-matched profile in Light and Jacobson (2002). The other mid-

441   latitude regions such as South Africa (Figure 6k) and southern Australia (Figure 6l) also have

442   enhanced activity at low altitudes, and low-level activity even dominates in mid-latitude regions

443   where a large fraction of the sources come from over the ocean - including the North Atlantic /

444   Mediterranean Sea (Figure 6b) and the northern Pacific Ocean (Figure 6c). The La Plata basin is

445   unique because its thunderstorms form over land where they may grow upscale into large

446   Mesoscale Convective Systems (MCSs) before moving offshore. Its altitude profile is heavily

447   weighted towards low-altitude sources, with a peak at 7 km. However, this is not due to the

448   contribution of oceanic thunderstorms. When the oceanic sources are removed, the peak only

449   increases to 8 km altitude.

450   There are a few potential explanations for the La Plata basin having such a low source

451   altitude profile. The most problematic would be contamination from South Atlantic Anomaly

452   (SAA) artifacts causing errors in the LLS source location. SAA artifacts manifest as single-pixel

453   detections or detections along a streak of pixels that are random and isolated in time to an

454   instrument like the LLS. Due to this randomness, they are not expected to consistently displace

455   the source location towards the center of the array where the altitude corresponding to a given

456   intra-pulse time difference would be lower (i.e., Figure 4a). Moreover, we can remove this

457   potential source of error by only plotting the intra-pulse time for each TIPP. When we replace

458   source altitude in Figure 6 with intra-pulse time, the La Plata basin altitude profile also has

459   smaller time delays between pulses, leading to a comparable shape to the altitude profile in

460   Figure 6j. The larger share of low-altitude VHF sources in the La Plata basin appears to be

461   legitimate.

462   We suggest that this increased fraction of low-altitude sources is due to the prevalence of

463   stratiform lightning. In addition to the upper positive charge layer, negative leaders also

464   propagate through regions of positive stratiform charge. However, while this propagation is

465   confined to a small area in convective cases, stratiform leaders can propagate over hundreds of

466   kilometers (Lang et al., 2017; Peterson, 2019; Lyons et al., 2020). Our previous analysis of an

467   oceanic megaflash in the FORTE record showed that the flash constantly emitted VHF radiation

468   in multiple periods of sequential triggering (i.e., series) that each lasted tens to hundreds of

469   milliseconds. The impulsive VHF sources that we could identify were clustered in a layer around

470   4-8 km altitude (Peterson et al., 2021a), consistent with Figure 6j. While megaflashes occur in

471   many regions, the La Plata basin is one of the primary Americas hotspots (Peterson, 2021;

472   Peterson and Stano, 2021) – along with the Continental United States, which also has an

473   increased share of low-altitude sources in Figure 6a. We have also recorded long horizontal

474   lightning over the Mediterranean Sea (Peterson et al., 2017a) (Figure 6b) and showed that the

475   remaining mid-latitude oceanic regions with increased low-altitude source fractions in Figure 6

476   are also locations with long horizontal flashes (Figure 5 in Peterson et al., 2017b).

477   The tropical regions in Figure 6, by contrast, are more heavily weighted towards higher

478   altitudes corresponding to the upper positive charge layer. However, the source altitude profiles

479   still different between these tropical regions. If we rank these regions by the 75th percentile VHF

480   source altitude, Panama / Colombia (Figure 6d) has the overall tallest thunderstorm charge

481   structures (13.6 km), followed by the Maritime Continent (Figure 6i; 13.0 km), the Continental

482   United States (12.6 km), and then the Congo Basin (Figure 6h; 12.6 km) and West Africa (Figure

483   6e; 12.5 km). The Amazon Basin (Figure 6g) has a nearly identical 75th percentile source altitude

484   as the joint India / the Indian Ocean region (Figure 6f) of 12.4 km in either case. The Amazon

485   has a larger share of low-altitude sources and, despite this higher 75th percentile altitude, the

486   mode is only at 10 km altitude.

487   Figure 7 maps these 75th percentile source altitudes (Figure 7a) for each gridpoint in

488   Figure 5 along with the median (Figure 7b) and 25th percentile (Figure 7c) values. Pixels with

489   less than 10 sources are not shown. The large regional domains used in Figure 6 obscure the fine-

490   scale structure caused by thunderstorm interactions with the local terrain. There is a marked

491   difference between the land-based and oceanic source altitude profiles. Tropical oceanic

492   thunderstorms can be just as tall as land-based storms over the Caribbean Sea, Gulf of Mexico,

493   Indian Ocean, and Pacific Ocean. At the same time, oceanic storms at higher latitudes (and in the

494   Atlantic Ocean between the Americas and Africa) tend to be quite shallow.

495   Much of the mid-latitude behavior is due to seasonal trends. Figure 8 shows latitude-

496   altitude profiles for land-based, the coastal ocean (within 1000 km of the continents) and the

497   open ocean (beyond 1000 km) averaged over 3-month periods. The profiles for each latitude are

498   normalized according to the total number of detected sources such that all columns in each panel

499   sum to 100%. The land-based source altitude profiles (left column) extend up to high altitudes

500   during the summer season with a dominant upper positive charge layer above 10 km. During the

501   winter, source altitudes are concentrated at lower altitudes around 5 km. The passage of the

502   seasons causes the summer upper and winter lower maxima to move in latitude, following the

503   increased insolation. The apparent slant in the distribution during northern hemisphere fall,

504   winter, and spring is due to the prevalence of low-altitude sources in the southern hemisphere

505   (i.e,. La Plata, South Africa, and Southern Australia) regions discussed previously. The coastal

506   ocean profiles, meanwhile, are similar to their land-based counterparts, and we can also see

507   similar seasonal behavior with the open ocean profiles (right column), though data is sparse from

508   these low flash rate thunderstorms far from shore.

509   3.3 Initiation and Propagation Altitudes in LLS Flashes

510   We previously demonstrated that FORTE is capable of documenting the evolution of

511   individual flashes (Peterson et al., 2021a,b). We used LLS to resolve the lateral development of

512   the leaders in the flash (as with LIS in Peterson et al., 2018) and then applied the altitude

513   algorithm to intracloud events that were identified and had their intra-pulse delays measured by

514   hand. In this section, we will follow the same procedure using pulses that were automatically

515   identified, linked, and assigned to LLS flashes.

516   An example of a particularly well-resolved flash is shown in Figure 9. Source altitudes

517   before (Figure 9a), during (Figure 9b), and after (Figure 9c) are shown for the flash of interest

518   (blue) and other flashes (red). We normal only consider isolated sources that do not have pulses

519   within 100 microseconds of the TIPP. However, to provide a more complete picture of VHF

520   activity in the flash, we show these potentially ambiguous sources in black in Figure 9b. The

521   extent of the LLS flash at each point in time is also overlaid as a line plot. VHF sources are

522   mapped in Figure 9d and colored according to whether they occurred in the flash of interest and

523   whether they occurred above or below 9 km altitude. Finally, a source altitude distribution is

524   shown in Figure 9e.

525   This flash case occurred in a thunderstorm over the Pacific Ocean on 7/12/2001. It started

526   with an RF-powerful TIPP at 7 km altitude followed promptly by activity in the upper positive

527   layer that was resolved by the LLS (line in Figure 9b). If we assume that these initial sources

528   bound the breakdown of the negative leader, then the approximate vertical speed of the

529   developing leader was $6.2x10^5$ ms^{-1}, which is consistent with the previously-reported vertical

530   speeds for negative leaders. Infrequent activity can also be noted in in a lower (apparently

531   negative) layer around 6 km altitude, and between the two layers. Since the first source from the

532   lower layer was ambiguous (black in Figure 9b), our filtered dataset would identify the first

533   activity in this lower activity as occurring 300 ms into the flash. Due to the low frequency of

534   sources from the lower negative layer, reductions in source counts from ambiguous negative

535   events have a greater impact on our statistics than positive sources. There were no other flashes

536   before the flash of interest, but a few were detected in the 30 s after it ended. These flashes had

537   similar altitude profiles (Figure 9e) to the flash of interest, with a high concentration of sources

538   around 12 km altitude and comparably few low-altitude sources.

539   Analyzing FORTE flashes like the cases in Figure 9 and Peterson et al. (2021a,b)

540   demonstrate that space-based platforms like FORTE are capable of resolving the flash

541   phenomena that are required for automatically resolving thunderstorm charge structure with

542   algorithms like chargepol. This was even demonstrated in Figure 21 Jacobson et al. (1999),

543   though a lack of geolocation information meant that the flash evolution was mapped in units of

544   intra-TIPP time rather than altitude. However, even the particularly well-resolved flash in Figure

545   9 also demonstrates the difficulties in applying these methods to on-orbit data. The first issue is

546   view time. Chargepol accumulates LMA data over time to derive the bulk electrical structure of

547   the thunderstorm. However, space-based platforms are only in view of a given thunderstorm for

548   a few minutes, and there might not be enough data during the overpass to generate robust

549   statistics – particularly from low flash rate oceanic storms. Another issue is that the level of

550   detail provided by a space-based platform is considerably less than what would be seen by a

551   typical LMA due to the increased range. Even in this case where we have dozens of sources

552   (which is rare), only 3 sources occur in the initial breakdown period (one of which is

553   ambiguous). There is not enough data to confidently resolve the upward propagation of the

554   negative leader in most FORTE flashes.

555   While we lack sufficient sources to characterize the initial breakdown of the negative

556   leader for individual flashes, we can still examine its statistical behavior by aggregating the

557   source altitude distributions from multiple flashes. Figure 10 computes the VHF cumulative

558   altitude distributions for each point in the durations of flashes over land (top row), over the

559   coastal ocean (middle row), and over the open ocean (bottom row). The left column uses linear

560   temporal bins to detail the initial 60 ms of the flash, while the right column accumulates data in

561   logarithmic bins out to 1 s after the flash start. Note that while these VHF sources are tied to

562   individual LLS flashes, the time of flash start is the time of the first RF source linked to the flash,

563   not the start of the optical emissions detected by the LLS. Median values are also indicated with

564   solid white lines.

565   The initial breakdown phase is evident as an increase in the overall source altitude

566   profiles over the first ~20 ms of the flash. This can be seen in flashes over land (Figure 10a), the

567   coastal ocean (Figure 10c) and the open ocean (Figure 10e), but with different slopes that should

568   correspond to the speed of the negative leader. If we fit the median altitude in the first 15 ms of

569   the flash to a linear model (black line), we get typical leader propagation speeds of 1.07×10^5 ms^{-1}

570   over land, 1.31×10^5 ms^{-1} over the coastal ocean, and 1.90×10^5 ms^{-1} over the open ocean. These

571   are all within the range reported by Shao and Krehbiel (1996). The apparent difference in

572   propagation speed between land and ocean regions is apparently linked to differences in flash

573   initiation altitude. Previous studies have noted cases of particularly fast negative leaders in

574   oceanic return strokes (for example, Wu et al., 2021). However, additional data is needed to

575   verify whether this trend is physical. After the initial breakdown period, the distributions become

576   flat, with little change in the source altitude profile over time (right column). While we see cases

577   of negative leaders sloping downward later in certain flashes (including the case in Figure 9), this

578   behavior does not occur in all flashes, and it occurs at random times where it is observed –

579   causing the lack of appreciable trend in the statistics.

580   The times in Figure 9 are based on the RF events that occurred during an LLS flash.

581   Figure 10, instead, computes the altitude profiles at each point relative to the first (left column)

582   and last (right column) LLS groups in the flash. We have shown previously that the most intense

583   optical emissions frequently occur in these first or last groups (Peterson and Rudlosky, 2019).

584   This is probably due to limitations on the types and altitudes of pulses that the pixelated lighting

585   imager can detect. LIS, for example, is known to trigger late in the flash while it is developing at

586   high altitudes (Thomas et al., 2000). There is no physical reason why the first LIS or LLS group

587   should rank as one of the most energetic pulses in the flash. However, if all of the early activity

588   in the flash leading up to the first pulse with comparable energy to a stroke is too faint to detect,

589   then bright events would cluster in the first group. We see in Figure 10a,c,d that the median RF

590   source altitudes before first light are around 10 km and there is no clear trend in the source

591   altitude distribution over time. This is consistent with the idea that the size and intensity of the

592   optical emitter, rather than its altitude, are the primary factors that contribute to this first

593   detection.

594   By contrast, the source altitudes relative to the end of the flash slope downwards over

595   time. The median source altitude associated with the final LLS group is close to 10 km in land

596   (Figure 11b) and coastal ocean (Figure 11d) regions – consistent with the approximate altitude

597   where optical coincidence was previously reported to fall off (Light and Jacobson, 2002). The

598   median source altitude at the time of the final LLS group in flashes over the open ocean is lower

599   at ~8 km, but the trend is otherwise similar to the land and coastal curves. We previously noted a

600   change in the behavior of LLS groups after the upper charge layer became apparently cut off

601   following the first return stroke in a hybrid CG flash (Peterson et al., 2021b). Before the stroke,

602   frequent dim emissions were detected as the flash developed through the upper charge layer.

603   This changed to only a few large and bright groups after the stroke when only the lower charge

604   layer was active. The statistics in Figure 11b,d,f suggest that the cessation of high-altitude

605   sources late in the flash is common in the FORTE record. Therefore, a likely explanation for the

606   final group in an LLS / LIS flash being particularly bright that it corresponds to the stroke or

607   other energetic process immediately before the high-altitude portions of the flash become cut off,

608   and any subsequent activity from the lower layer is too dim for the imager to detect.

609   Finally, we compute the initiation and propagation altitudes for these FORTE flashes. To

610   allow for errors from spurious sources, we define the initiation altitude as the lowest altitude of

611   all sources during the initial breakdown phase within 15 ms of the flash start. Then, the

612   propagation altitude is defined as the average altitude of all sources in the LLS flash. For this

613   analysis, we will allow the ambiguous sources (black dots in 10b) to better resolve activity in the

614   negative charge layer. Profiles of initiation altitude (left column) and propagation altitude (right

615   column) are shown in Figure 12 for flashes over land (top row), the coastal ocean (middle row)

616   and the open ocean (bottom row).

617   The initiation altitude profile for land-based flashes has two peaks: a lower peak at 7 km

618   altitude, and an upper peak at 10-11 km altitude. Oceanic flashes are more likely to have their

619   initial sources at low altitudes, as we saw in Figure 12. The lower peak (6 km altitude) is

620   dominant over the upper peak for the coastal ocean (Figure 12c), while the upper peak is hardly

621   apparent for flashes over the open ocean (Figure 12e) where the lower peak is further reduced to

622   4 km altitude. The peaks in the propagation altitude distribution, meanwhile, are similar between

623   land and the coastal ocean, though the oceanic flashes are still more likely to propagate at lower

624   altitudes, overall. The propagation altitude profile for flashes over the open ocean is single-

625   peaked with a maximum at 7 km altitude.

626   These altitude profiles do not consider variations in flash initiation or propagation

627   altitudes by flash type (intracloud or Cloud to Ground) or storm type (as in Mecikalski and

628   Carey, 2018), which jointly vary by region of the Earth. Flash type and storm type partitioning

629   are topics that we plan to consider in future work.

630

5 Conclusion

632   We leverage coincident detections of lightning events by the FORTE RF system and LLS

633   to document the altitude distributions of in-cloud lightning sources across the globe. Previous

634   FORTE studies generated profiles of VHF source altitudes (Light and Jacobson, 2002) but were

635   limited by a small sample size. Using the full FORTE RF record and relaxing the criteria for LLS

636   coincidence, we are able to characterize the vertical distributions of VHF sources over large

637   swaths of the Earth's land and ocean regions.

638   The negative leaders that are prevalent emitters of VHF radiation most often propagate

639   through the upper positive charge layer of ordinary thunderstorms. For this reason, the FORTE

640   VHF source altitude distributions generally peak at 11 km altitude. However, VHF sources at

641   lower altitudes including initial breakdowns and later activity in the lower negative charge layer

642   can also resolved from space. We also find that typical vertical development speeds of these

643   negative leaders appear to differ between land (1.07×10^5 ms^{-1}), coastal oceanic regions (1.31×10^5

644   ms^{-1}), and the open ocean (1.90×10^5 ms^{-1}). However, while FORTE can resolve the lightning

645   phenomena required for automated charge layer identification with the chargepol algorithm

646   (Medina et al., 2021), the level of unambiguous detail we can resolve is usually not sufficient to

647   characterize the upward developing leader on a per-flash basis, and the limited viewtime

648   provided by its Low Earth Orbit (LEO) inhibits robust statistics from individual thunderstorms.

649   Low-altitude sources are found to be particularly common in winter and/or oceanic

650   regions outside of the tropics, as well as over the La Plata basin where large MCSs produce

651   abundant stratiform lightning including megaflashes. We previously showed that an individual

652   large stratiform flash can produce hundreds of FORTE RF events with their impulsive VHF

653   sources clustered in a layer between 4 and 8 km altitude (Peterson et al., 2021a). Regions with

654   frequent stratiform lightning are thus expected to have significant contributions from both high-

655   altitude convective sources and low-altitude stratiform sources. Tropical regions, meanwhile, had

656   the tallest source altitude profiles with the Colombia and Panama region having the greatest 75th

657   percentile source altitude (13.6 km) of the regions considered.

658   Regional factors including seasonal variations in storm type are shown to have a

659   pronounced impact on the VHF source altitude profiles as well as the initiation and propagation

660   heights of individual flashes. We provide a high-level overview of some of the variations in the

661   data, but further in-depth analysis is required to explain all of the trends in this new dataset. We

662   also plan to create distinct altitude profiles for CG and IC flashes as well as various storm types

663   (as in Mecikalski and Carey, 2018) in future work. It is expected that these global measurements

664   will be valuable for global climate modeling, particularly LNOx models, that currently derive

665   lightning altitudes from parameterizations based on environmental parameters. Further

666   applications of this data will also be explored in future work.

667

Open Research

669   The FORTE data used in this study are available at the Harvard Dataverse and may be accessed

670   via the DOI listed in Peterson (2022).

671 **Acknowledgments**

677

678

References

679

680

681   Albrecht, R. I., Goodman, S. J., Buechler, D. E., Blakeslee, R. J., & Christian, H. J. (2016).

682   Where are the lightning hotspots on Earth?. *Bulletin of the American Meteorological*

683   *Society*, *97*(11), 2051-2068.

684   Bitzer, P. M. (2017). Global distribution and properties of continuing current in lightning.

685   *Journal of Geophysical Research: Atmospheres*, *122*(2), 1033-1041.

686   Carey, L. D., Koshak, W., Peterson, H., & Mecikalski, R. M. (2016). The kinematic and

687   microphysical control of lightning rate, extent, and NOX production. *Journal of*

688   *Geophysical Research: Atmospheres*, *121*(13), 7975-7989.

689   Cecil, D. J., Buechler, D. E., & Blakeslee, R. J. (2014). Gridded lightning climatology from

690   TRMM-LIS and OTD: Dataset description. *Atmospheric Research*, *135*, 404-414.

691   Chameides, W., & Walker, J. C. (1973). A photochemical theory of tropospheric ozone. *Journal*

692   *of Geophysical Research*, *78*(36), 8751-8760.

693   Christian, H. J., R. J. Blakeslee, S. J. Goodman, and D. M. Mach (Eds.), 2000: Algorithm

694   Theoretical Basis Document (ATBD) for the Lightning Imaging Sensor (LIS),

695   NASA/Marshall Space Flight Center, Alabama. (Available as

696   http://eospso.gsfc.nasa.gov/atbd/listables.html, posted 1 Feb. 2000)

697   Crutzen, P. (1973). A discussion of the chemistry of some minor constituents in the stratosphere

698   and troposphere. *Pure and Applied Geophysics*, *106*(1), 1385-1399.

699   Crutzen, P. J., Heidt, L. E., Krasnec, J. P., Pollock, W. H., & Seiler, W. (1979). Biomass burning

700   as a source of atmospheric gases CO, H2, N2O, NO, CH3Cl and COS. *Nature*,

701   *282*(5736), 253-256.

702   Cummins, K. L., Murphy, M. J., Bardo, E. A., Hiscox, W. L., Pyle, R. B., & Pifer, A. E. (1998).

703   A combined TOA/MDF technology upgrade of the US National Lightning Detection

704   Network. *Journal of Geophysical Research: Atmospheres*, *103*(D8), 9035-9044.

705   DeCaria, A. J., Pickering, K. E., Stenchikov, G. L., Scala, J. R., Stith, J. L., Dye, J. E., ... &

706   Laroche, P. (2000). A cloud-scale model study of lightning-generated NO x in an

707   individual thunderstorm during STERAO-A. *Journal of Geophysical Research:*

708   *Atmospheres*, *105*(D9), 11601-11616.

709   Ely, B. L., Orville, R. E., Carey, L. D., & Hodapp, C. L. (2008). Evolution of the total lightning

710   structure in a leading-line, trailing-stratiform mesoscale convective system over Houston,

711   Texas. *Journal of Geophysical Research: Atmospheres*, *113*(D8).

712   Fierro, A. O., Shao, X. M., Hamlin, T., Reisner, J. M., & Harlin, J. (2011). Evolution of eyewall

713   convective events as indicated by intracloud and cloud-to-ground lightning activity

714   during the rapid intensification of hurricanes Rita and Katrina. *Monthly Weather Review*,

715   *139*(5), 1492-1504.

716   Fishman, J., Solomon, S., & Crutzen, P. J. (1979). Observational and theoretical evidence in

717   support of a significant in-situ photochemical source of tropospheric ozone. *Tellus*, *31*(5),

718   432-446.

719   Ivanov, M. F., Kiverin, A. D., Klumov, B. A., & Fortov, V. E. (2014). From combustion and

720   detonation to nitrogen oxides. *Physics-Uspekhi*, *57*(3), 234.

721   Jacobson, A. R., Knox, S. O., Franz, R., & Enemark, D. C. (1999). FORTE observations of

722   lightning radio-frequency signatures: Capabilities and basic results. *Radio Science*, *34*(2),

723   337-354.

724   Jaeglé, L., Jacob, D. J., Wang, Y., Weinheimer, A. J., Ridley, B. A., Campos, T. L., ... & Hagen,

725   D. E. (1998). Sources and chemistry of NOx in the upper troposphere over the United

726   States. *Geophysical Research Letters*, *25*(10), 1705-1708.

727   Jayaratne, E. R., Saunders, C. P. R., & Hallett, J. (1983). Laboratory studies of the charging of

728   soft-hail during ice crystal interactions. *Quarterly Journal of the Royal Meteorological*

729   *Society*, *109*(461), 609-630.

730   Kirkland, M. W., Suszcynsky, D. M., Guillen, J. L. L., & Green, J. L. (2001). Optical

731   observations of terrestrial lightning by the FORTE satellite photodiode detector. *Journal*

732   *of Geophysical Research: Atmospheres*, *106*(D24), 33499-33509.

733   Labrador, L. J., Von Kuhlmann, R., & Lawrence, M. G. (2005). The effects of lightning-

734   produced NO x and its vertical distribution on atmospheric chemistry: sensitivity

735   simulations with MATCH-MPIC. *Atmospheric Chemistry and Physics*, *5*(7), 1815-1834.

736   Lacis, A. A., Wuebbles, D. J., & Logan, J. A. (1990). Radiative forcing of climate by changes in

737   the vertical distribution of ozone. *Journal of Geophysical Research: Atmospheres*,

738   *95*(D7), 9971-99

739   Lang, T. J., & Rutledge, S. A. (2008). Kinematic, microphysical, and electrical aspects of an

740   asymmetric bow-echo mesoscale convective system observed during STEPS 2000.

741   *Journal of Geophysical Research: Atmospheres*, *113*(D8).

742   Lang, T. J., Pédeboy, S., Rison, W., Cerveny, R. S., Montanyà, J., Chauzy, S., ... & Krahenbuhl,

743   D. S. (2017). WMO world record lightning extremes: Longest reported flash distance and

744   longest reported flash duration. *Bulletin of the American Meteorological Society*, *98*(6),

745   1153-1168.

746   Light, T. E. L., & Jacobson, A. R. (2002). Characteristics of impulsive VHF lightning signals

747   observed by the FORTE satellite. *Journal of Geophysical Research: Atmospheres*,

748   *107*(D24), ACL-8.

749   Luo, C., Wang, Y., & Koshak, W. J. (2017). Development of a self-consistent lightning NOx

750   simulation in large-scale 3-D models. *Journal of Geophysical Research: Atmospheres*,

751   *122*(5), 3141-3154.

752   López, J. A., Montanyà, J., van der Velde, O. A., Pineda, N., Salvador, A., Romero, D., ... &

753   Taborda, J. (2019). Charge structure of two tropical thunderstorms in Colombia. *Journal*

754   *of Geophysical Research: Atmospheres*, *124*(10), 5503-5515.

755   Lyons, W. A., Bruning, E. C., Warner, T. A., MacGorman, D. R., Edgington, S., Tillier, C., &

756   Mlynarczyk, J. (2020). Megaflashes: Just how long can a lightning discharge get?.

757   *Bulletin of the American Meteorological Society*, *101*(1), E73-E86.

758   Mach, D. M., Christian, H. J., Blakeslee, R. J., Boccippio, D. J., Goodman, S. J., & Boeck, W. L.

759   (2007). Performance assessment of the optical transient detector and lightning imaging

760   sensor. *Journal of Geophysical Research: Atmospheres*, *112*(D9).

761   Marshall, T. C., & Rust, W. D. (1991). Electric field soundings through thunderstorms. *Journal*

762   *of Geophysical Research: Atmospheres*, *96*(D12), 22297-22306.

763   Marshall, T. C., Rust, W. D., Winn, W. P., & Gilbert, K. E. (1989). Electrical structure in two

764   thunderstorm anvil clouds. *Journal of Geophysical Research: Atmospheres*, *94*(D2),

765   2171-2181.

766   Mansell, E. R., MacGorman, D. R., Ziegler, C. L., & Straka, J. M. (2005). Charge structure and

767   lightning sensitivity in a simulated multicell thunderstorm. *Journal of Geophysical*

768   *Research: Atmospheres*, *110*(D12).

769   Mecikalski, R. M., & Carey, L. D. (2018). Radar reflectivity and altitude distributions of

770   lightning as a function of IC, CG, and HY flashes: Implications for LNOx production.

771   *Journal of Geophysical Research: Atmospheres*, *123*(22), 12-796.

772   Peterson, M. (2019). Research applications for the Geostationary Lightning Mapper operational

773   lightning flash data product. *Journal of Geophysical Research: Atmospheres*, *124*(17-18),

774   10205-10231.

775   Peterson, M. (2021). Where are the most extraordinary lightning megaflashes in the Americas?.

776   *Bulletin of the American Meteorological Society*, *102*(3), E660-E671.

777   Peterson, M. (2022). FORTE Lightning Altitude Data, https://doi.org/10.7910/DVN/0ZWPTL,

778   Harvard Dataverse, DRAFT VERSION

779   Peterson, M., & Rudlosky, S. (2019). The time evolution of optical lightning flashes. *Journal of*

780   *Geophysical Research: Atmospheres*, *124*(1), 333-349.

781   Peterson, M., & Stano, G. (2021). The Hazards Posed by Mesoscale Lightning Megaflashes.

782   *Earth Interactions*, *25*(1), 46-56.

783   Peterson, M., Rudlosky, S., & Deierling, W. (2017a). The evolution and structure of extreme

784   optical lightning flashes. *Journal of Geophysical Research: Atmospheres*, *122*(24), 13-

785   370.

786   Peterson, M., Deierling, W., Liu, C., Mach, D., & Kalb, C. (2017b). The properties of optical

787   lightning flashes and the clouds they illuminate. *Journal of Geophysical Research:*

788   *Atmospheres*, *122*(1), 423-442.

789   Peterson, M., Rudlosky, S., & Deierling, W. (2018). Mapping the lateral development of

790   lightning flashes from orbit. *Journal of Geophysical Research: Atmospheres*, *123*(17),

791   9674-9687.

792   Peterson, M., Light, T. E., & Shao, X. M. (2021a). Combined Optical and Radio-Frequency

793   Measurements of a Lightning Megaflash by the FORTE Satellite. *Journal of Geophysical*

794   *Research: Atmospheres*, *126*(15), e2020JD034411.

795   Peterson, M., Light, T. E. L., & Shao, X.-M. (2021b). Combined optical and radio-frequency

796   perspectives on a hybrid Cloud-to-Ground lightning flash observed by the FORTE

797   satellite. *Journal of Geophysical Research: Atmospheres*, 126, e2020JD034152.

798   https://doi.org/10.1029/2020JD034152

799   Peterson, M., Mach, D., & Buechler, D. (2021c). A Global LIS/OTD Climatology of Lightning

800   Flash Extent Density. *Journal of Geophysical Research: Atmospheres*, *126*(8),

801   e2020JD033885.

802   Pickering, K. E., Wang, Y., Tao, W. K., Price, C., & Müller, J. F. (1998). Vertical distributions

803   of lightning NOx for use in regional and global chemical transport models. *Journal of*

804   *Geophysical Research: Atmospheres*, *103*(D23), 31203-31216.

805   Rakov, V. A., & Uman, M. A. (2003). *Lightning: physics and effects*. Cambridge university

806   press.

807   Reynolds, S. E., Brook, M., & Gourley, M. F. (1957). Thunderstorm charge separation. Journal

808   of Meteorology, 14(5), 163–178.

809   Rison, W., Thomas, R. J., Krehbiel, P. R., Hamlin, T., & Harlin, J. (1999). A GPS-based three-

810   dimensional lightning mapping system: Initial observations in central New Mexico.

811   *Geophysical research letters*, *26*(23), 3573-3576.

812   Saunders, C. P. R., & Peck, S. L. (1998). Laboratory studies of the influence of the rime

813   accretion rate on charge transfer during crystal/graupel collisions. *Journal of Geophysical*

814   *Research: Atmospheres*, *103*(D12), 13949-13956.

815   Saunders, C. P. R., Keith, W. D., & Mitzeva, R. P. (1991). The effect of liquid water on

816   thunderstorm charging. *Journal of Geophysical Research: Atmospheres*, *96*(D6), 11007-

817   11017.

818   Schuur, T. J., & Rutledge, S. A. (2000). Electrification of stratiform regions in mesoscale

819   convective systems. Part I: An observational comparison of symmetric and asymmetric

820   MCSs. *Journal of the atmospheric sciences*, *57*(13), 1961-1982.

821   Seiler, W., & Crutzen, P. J. (1980). Estimates of gross and net fluxes of carbon between the

822   biosphere and the atmosphere from biomass burning. *Climatic change*, *2*(3), 207-247.

823   Shao, X. M., & Krehbiel, P. R. (1996). The spatial and temporal development of intracloud

824   lightning. *Journal of Geophysical Research: Atmospheres*, *101*(D21), 26641-26668.

825   Simpson, G. C., & Scrase, F. J. (1937). The distribution of electricity in thunderclouds.

826   *Proceedings of the Royal Society of London. Series A-Mathematical and Physical*

827   *Sciences*, *161*(906), 309-352.

828   Smith, D. A., Heavner, M. J., Jacobson, A. R., Shao, X. M., Massey, R. S., Sheldon, R. J., &

829   Wiens, K. C. (2004). A method for determining intracloud lightning and ionospheric

830   heights from VLF/LF electric field records. *Radio Science*, *39*(1), 1-11.

831   Stolzenburg, M., Rust, W. D., Smull, B. F., & Marshall, T. C. (1998). Electrical structure in

832   thunderstorm convective regions: 1. Mesoscale convective systems. *Journal of*

833   *Geophysical Research: Atmospheres*, *103*(D12), 14059-14078.

834   Suszcynsky, D. M., & Heavner, M. J. (2003). Narrow bipolar events as indicators of

835   thunderstorm convective strength. *Geophysical research letters*, *30*(17).

836   Suszcynsky, D. M., Kirkland, M. W., Jacobson, A. R., Franz, R. C., Knox, S. O., Guillen, J. L.

837   L., & Green, J. L. (2000). FORTE observations of simultaneous VHF and optical

838   emissions from lightning: Basic phenomenology. *Journal of Geophysical Research:*

839   *Atmospheres*, *105*(D2), 2191-2201.

840   Suszcynsky, D. M., Light, T. E., Davis, S., Green, J. L., Guillen, J. L. L., & Myre, W. (2001).

841   Coordinated observations of optical lightning from space using the FORTE photodiode

842   detector and CCD imager. *Journal of Geophysical Research: Atmospheres*, *106*(D16),

843   17897-17906.

844   Takahashi, T. (1978). Riming electrification as a charge generation mechanism in thunderstorms.

845   *Journal of Atmospheric Sciences*, *35*(8), 1536-1548.

846   Takahashi, T., & Miyawaki, K. (2002). Reexamination of riming electrification in a wind tunnel.

847   *Journal of the Atmospheric Sciences*, *59*(5), 1018-1025.

848   Thomas, R. J., Krehbiel, P. R., Rison, W., Hamlin, T., Boccippio, D. J., Goodman, S. J., &

849   Christian, H. J. (2000). Comparison of ground-based 3-dimensional lightning mapping

850   observations with satellite-based LIS observations in Oklahoma. *Geophysical research*

851   *letters*, *27*(12), 1703-1706.

852   Thomas, R. J., Krehbiel, P. R., Rison, W., Hunyady, S. J., Winn, W. P., Hamlin, T., & Harlin, J.

853   (2004). Accuracy of the lightning mapping array. *Journal of Geophysical Research:*

854   *Atmospheres*, *109*(D14).

855   Tie, X., Zhang, R., Brasseur, G., & Lei, W. (2002). Global NOx production by lightning. *Journal*

856   *of Atmospheric Chemistry*, *43*(1), 61-74.

857   Williams, E. R. (1989). The tripole structure of thunderstorms. *Journal of Geophysical*

858   *Research: Atmospheres*, *94*(D11), 13151-13167.

859   Williams, E. (2018). Lightning activity in winter storms: A meteorological and cloud

860   microphysical perspective. *IEEJ Transactions on Power and Energy*, *138*(5), 364-373.

861 Wilson, C. T. R. (1920). III. Investigations on lightning discharges and on the electric field of

862   thunderstorms. *Philosophical Transactions of the Royal Society of London. Series A,*

863   *Containing Papers of a Mathematical or Physical Character*, *221*(582-593), 73-115.

864 Wu, T., Wang, D., Huang, H., & Takagi, N. (2021). The strongest negative lightning strokes in

865   winter thunderstorms in Japan. *Geophysical Research Letters*, *48*(21), e2021GL095525.

866 Yamamoto, M. K., Higuchi, A., & Nakamura, K. (2006). Vertical and horizontal structure of

867   winter precipitation systems over the western Pacific around Japan using TRMM data.

868   *Journal of Geophysical Research: Atmospheres*, *111*(D13).

869 Zheng, D., Wang, D., Zhang, Y., Wu, T., & Takagi, N. (2019). Charge regions indicated by

870   LMA lightning flashes in Hokuriku's winter thunderstorms. *Journal of Geophysical*

871   *Research: Atmospheres*, *124*(13), 7179-7206.

872

873 **Table 1.** Variations in RF pulse feature counts after successively applying each filter. The final 2
874 filters are only applied for the analyses in Section 3.3 and the Supporting Information (SI).
875

	All Pulses	TIPPs	TIPPS w/LLS Coincidence
No Filters	3,089,812	1,096,885	380,347
Valid TEC	2,694,726	1,006,466	330,302
Centered in Record	2,437,408	907,083	300,214
Isolated in Time	1,796,217	695,146	202,062
1 Active LLS Area	-	-	152,955
1 Active LLS Flash	-	-	130,261

876
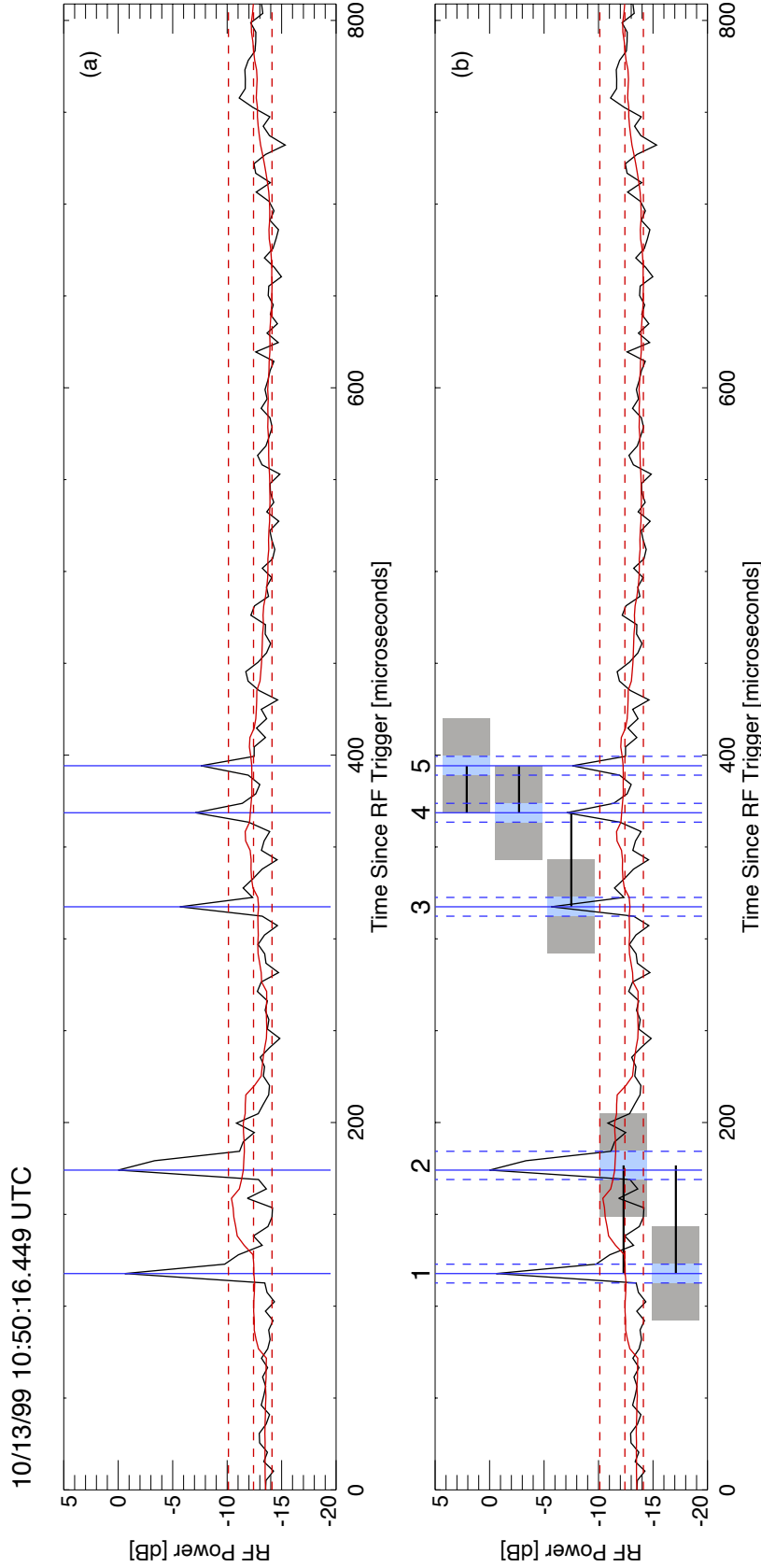
Figure 1. Example RF event record with multiple identified pulses. Peak (solid blue vertical lines) and pulse (blue bars between dashed blue lines) features are identified from contiguous regions of the original power timeseries (black curve) that are 3 standard deviations (horizontal dashed lines) above the minimum of the smoothed timeseries (red curve), as described in text. Pulse windows used to compute their properties (grey bars) and links between pairs of impulsive events (horizontal black lines) are also shown.

911

912
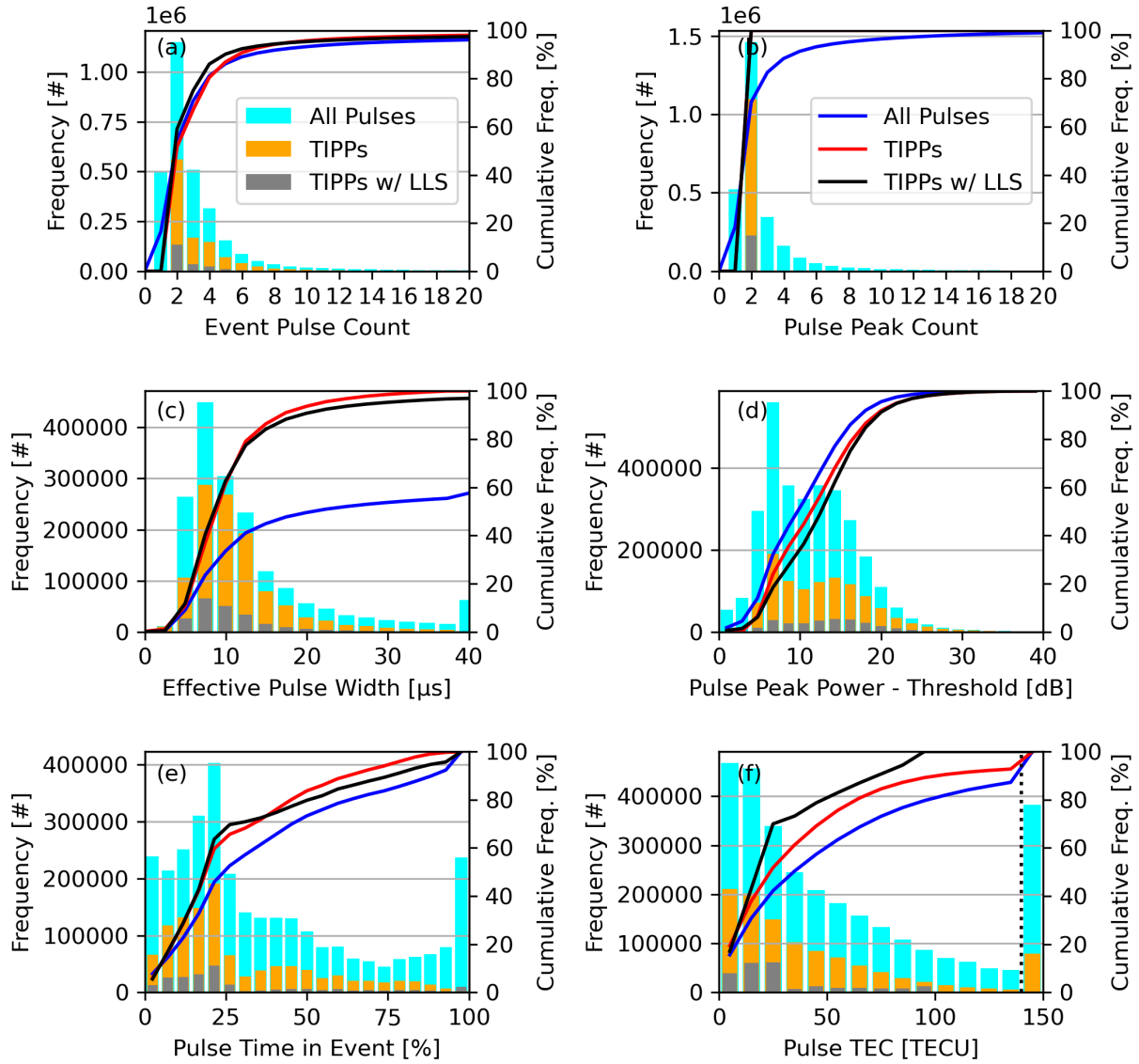
913
914
915 **Figure 2.** Histograms and cumulative distributions of (a) the number of pulses per event, (b) the
916 number of peaks per pulse, (c) the effective pulse with, (d) the peak power above the threshold,
917 (e) the time of the pulse in the event record, and (f) the TEC experienced by the pulse reported
918 by the dechirping algorithm. Separate distributions are shown for all pulses, TIPPs, and TIPPs
919 that also have LLS coincidence at the flash level.
920

FORTE Satellite Subpoint Locations during RF Events with Pulses

FORTE Satellite Subpoint Locations during RF Pulses

FORTE Satellite Subpoint Locations during RF TIPPs
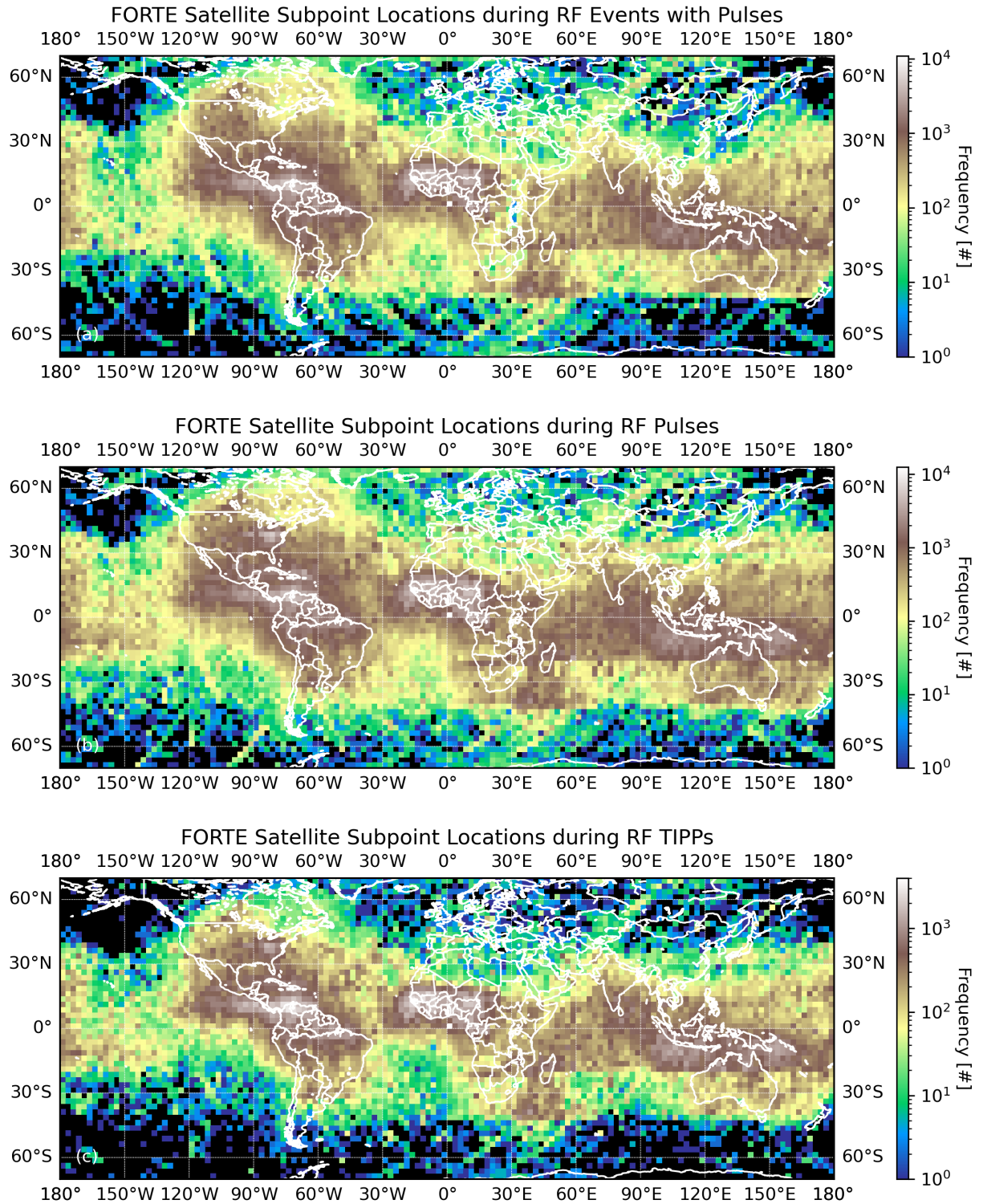
Figure 3. Global distributions of the FORTE satellite subpoint position during (a) RF events containing pulse features, (b) RF pulse features, and (c) RF TIPPs.
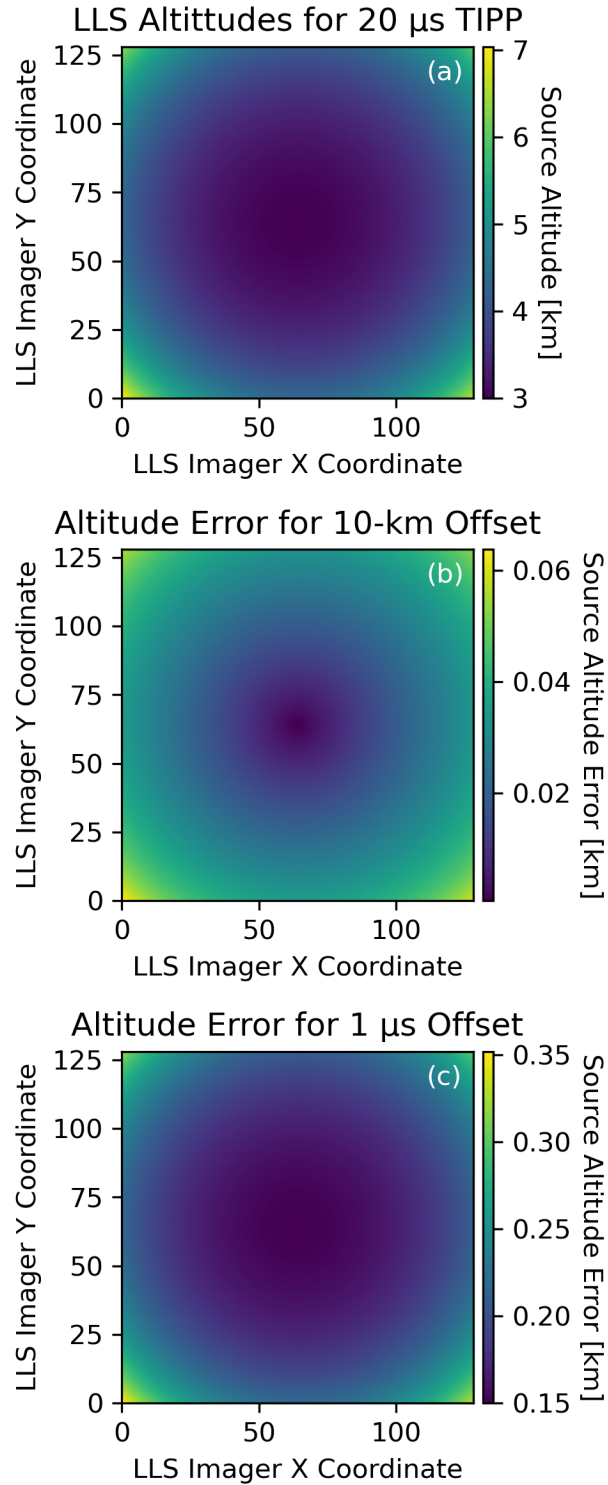
925
926 **Figure 4.** Distributions of altitude (a) and altitude error (b-c) for a TIPP with a 20 microsecond
927 intra-pulse time interval located at each LLS imager pixel. (b) The altitude error from the
928 detected VHF source being displaced 10 km radially outward from its true location. (c) The
929 altitude error from the intra-pulse time interval being off by 1 microsecond.
930
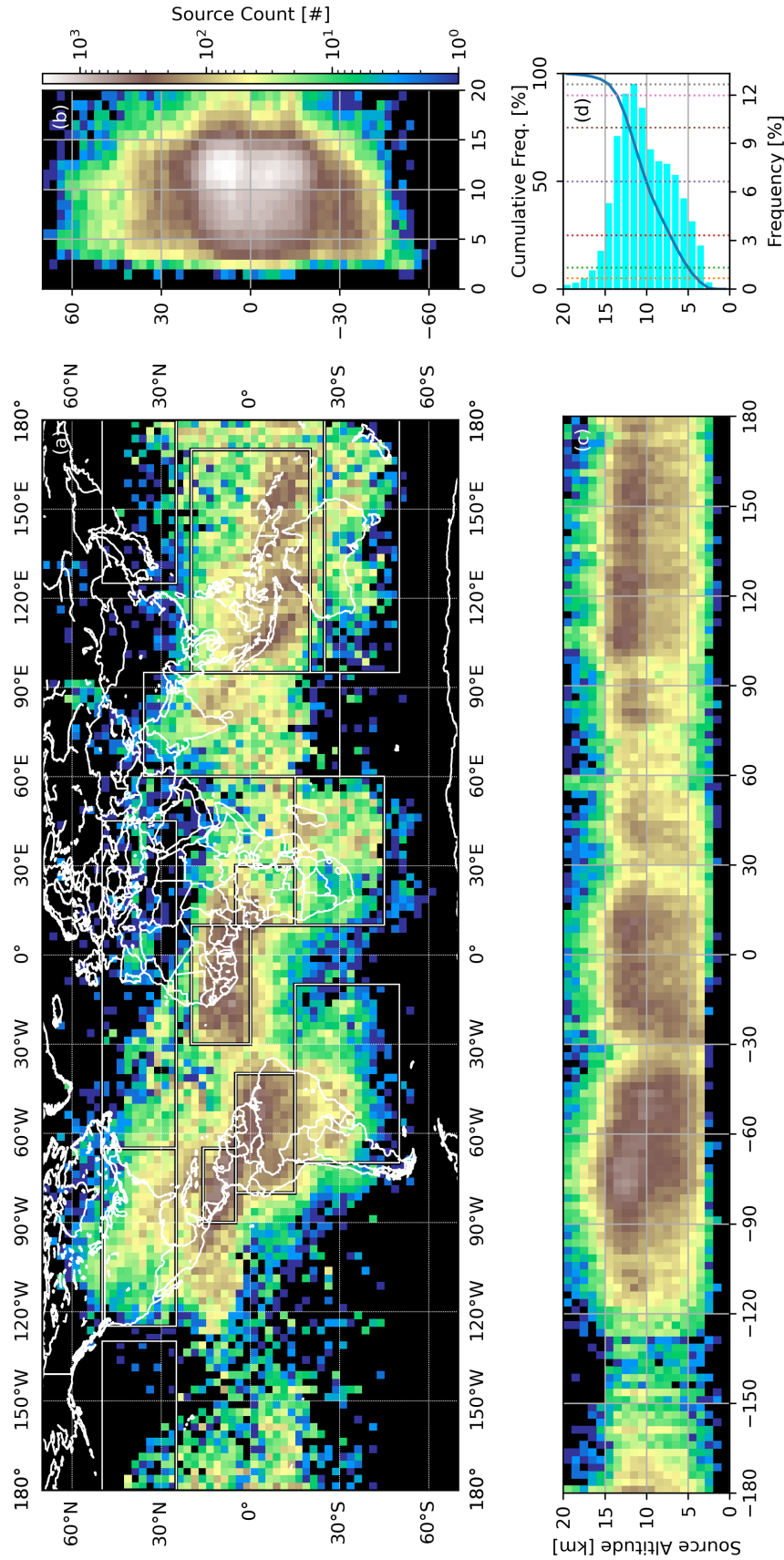
Figure 5. Distributions of LLS-coincident VHF sources. (a) Geographic distribution of VHF sources with regions of interest boxed. (b) Latitude-altitude source distribution. (c) Longitude-altitude distribution. (d) Global source altitude histogram (bars) and cumulative distribution (solid line).

931
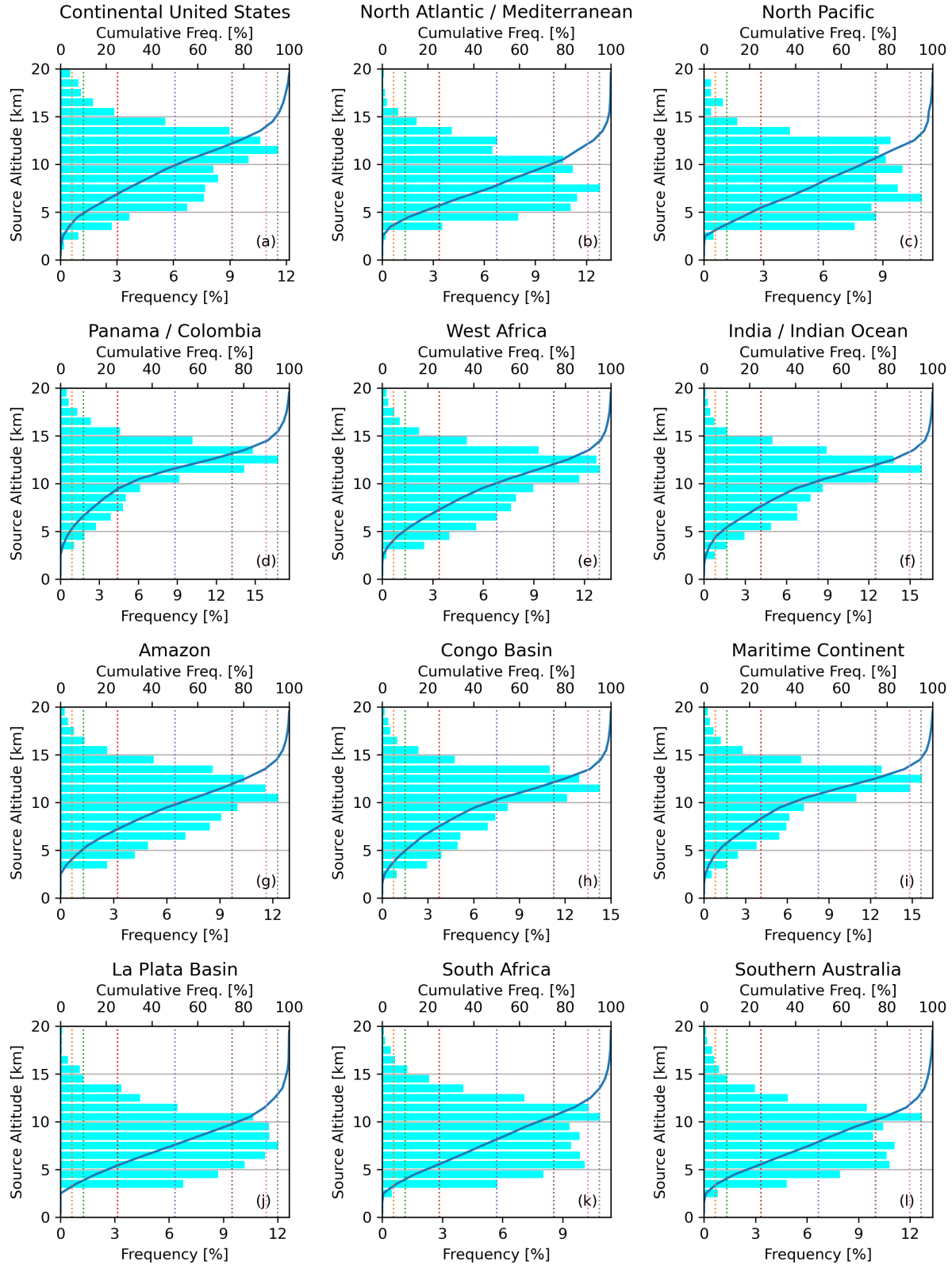
Figure 6. VHF source altitude profile for the regions boxed in Figure 5 organized by longitude (columns) and latitude (rows).
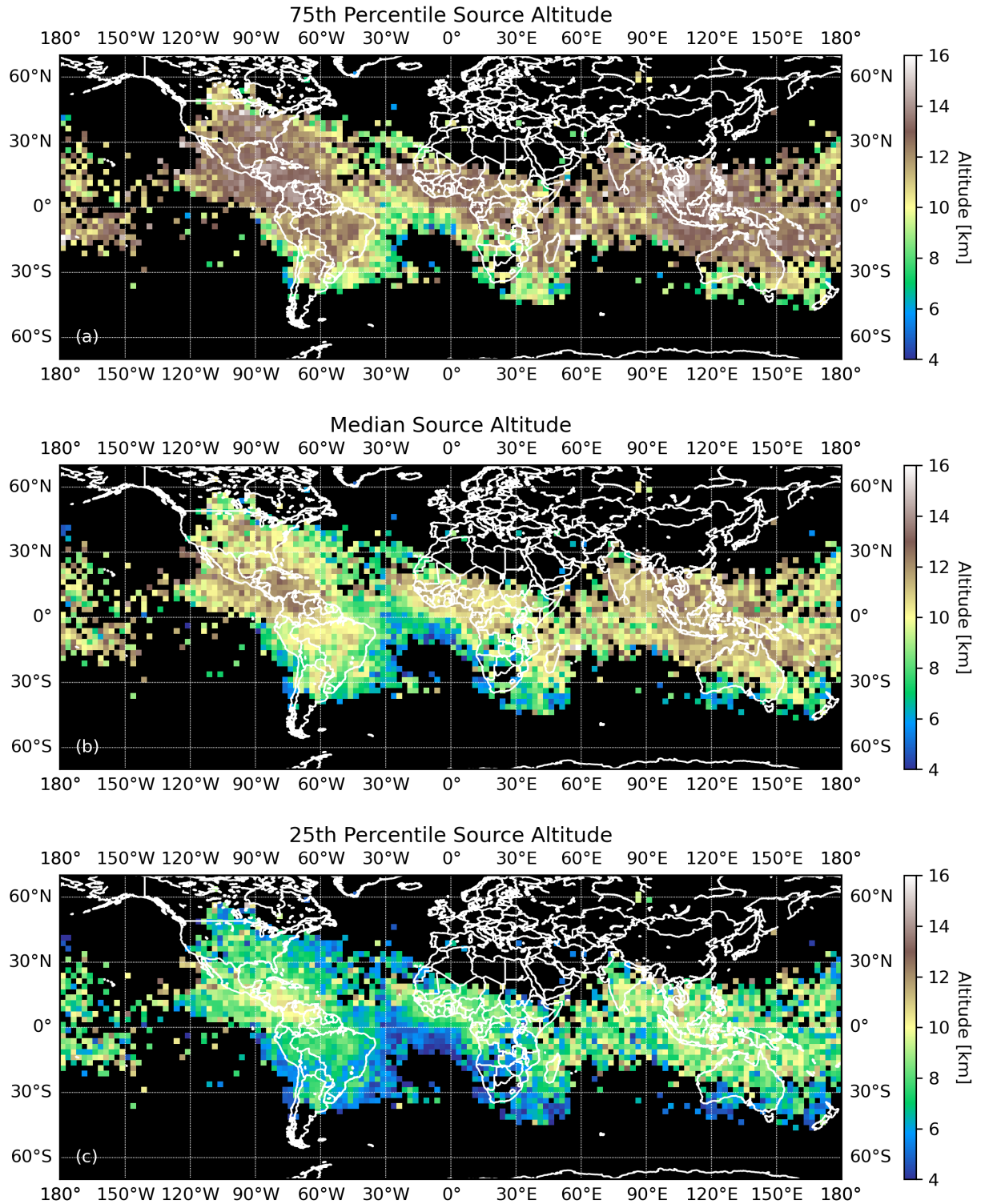
Figure 7. Global maps of (a) 75th percentile, (b) median, and (c) 25th percentile source altitudes.

938
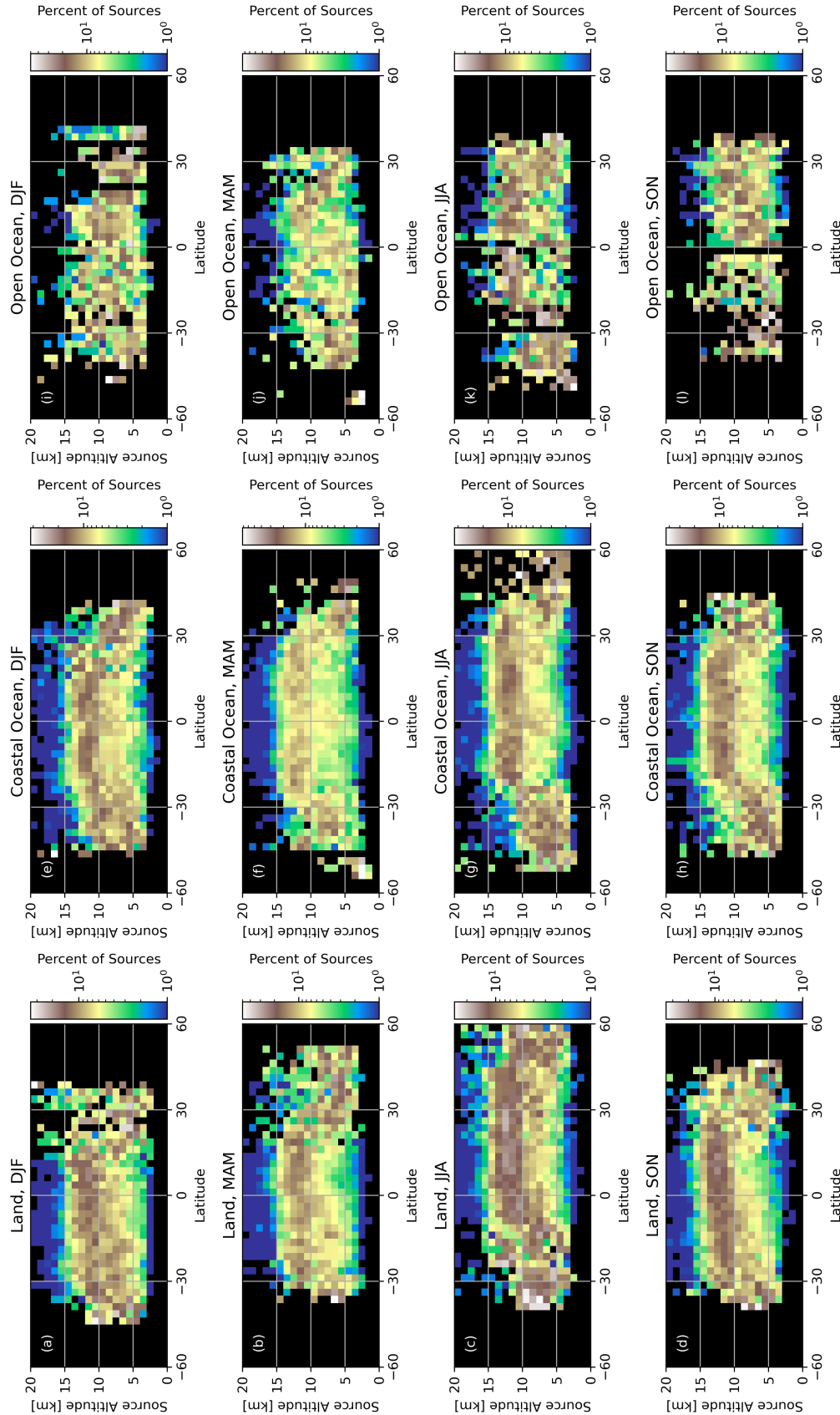
Figure 8. Latitude-altitude distributions of VHF sources detected over land (left), the coastal ocean (center), and the open ocean (right) during December-February (top row), March-May (second row), June – August (third row), and September – November (bottom row).
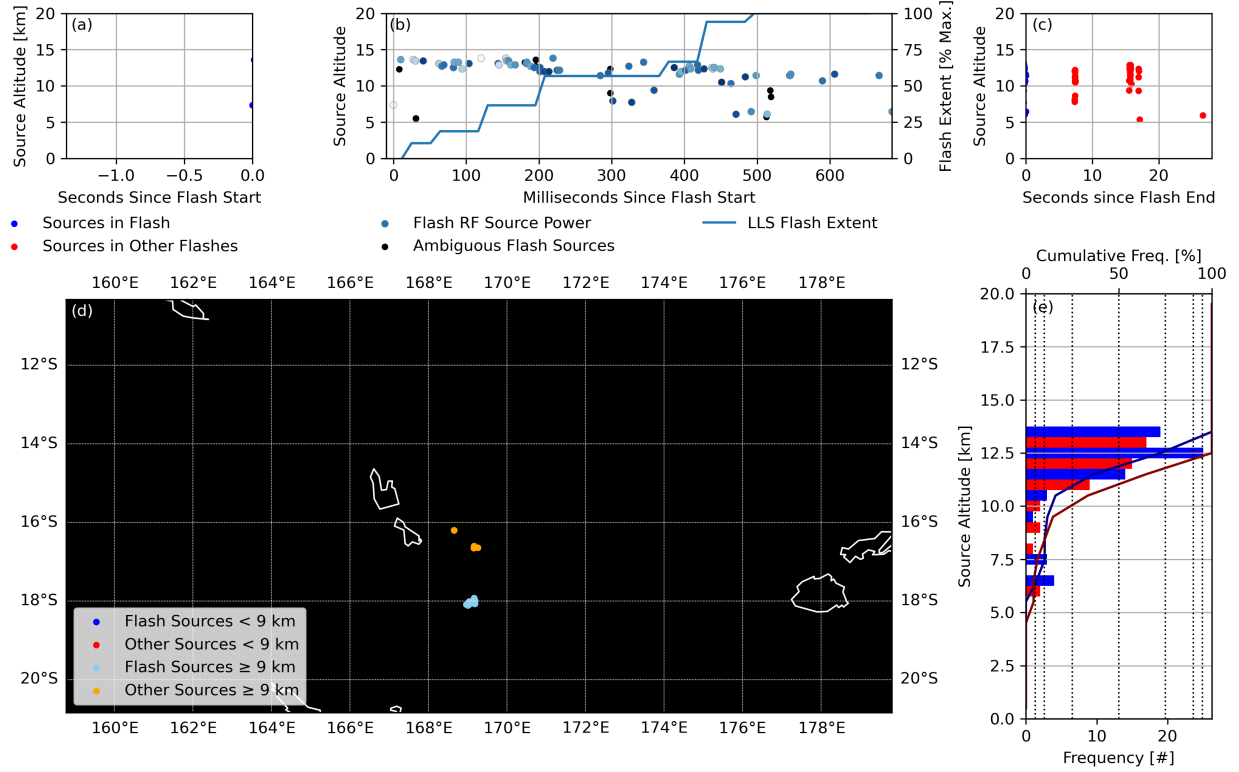
Figure 9. Altitude timeseries of source altitudes (a) before, (b) during, and (c) after an LLS flash of interest. Sources that were part of the flash are shown in blue, while sources in other flashes are shown in red. The locations of these sources are mapped in (d), and their vertical profiles are shown in (e). The blue color scale in (b) denotes RF power from minimum (dark blue) to maximum (white). Sources with ambiguous TIPP links are denoted with black in (b). Sources in (d) are shaded according to altitude.
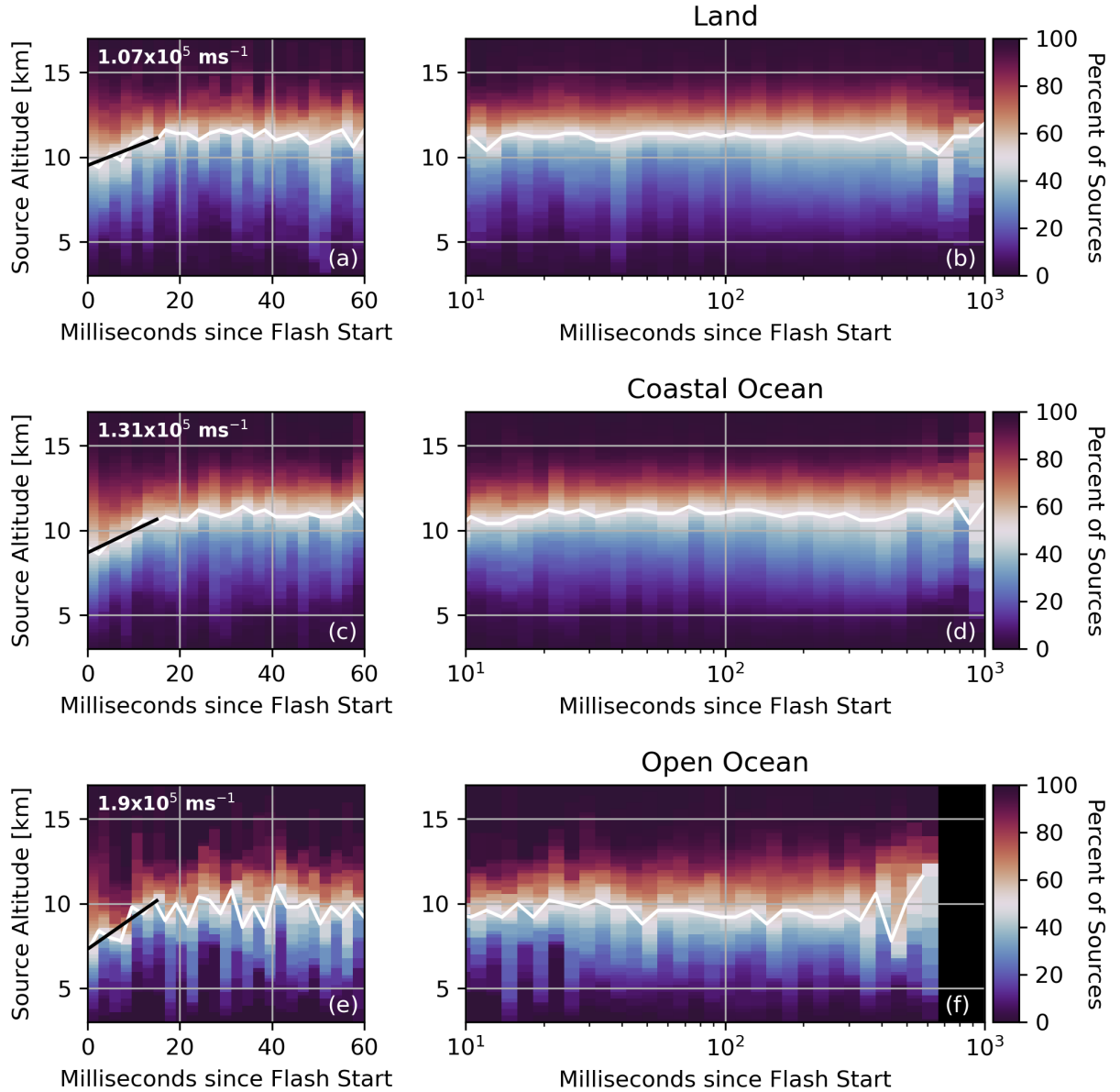
Figure 10. Cumulative distributions of source attitude at each point over the duration of land (top row), coastal ocean (middle row) and open ocean (bottom) flashes. Early activity in the flash is shown with linear temporal bins in the left column, while the full flash duration is shown with logarithmic temporal bins in the right column. Linear fits to the median altitude in the first 15 ms of the flashes are shown with black lines whose slope approximates typical vertical propagation speeds (listed at the top of the plot) for negative leaders in each region.
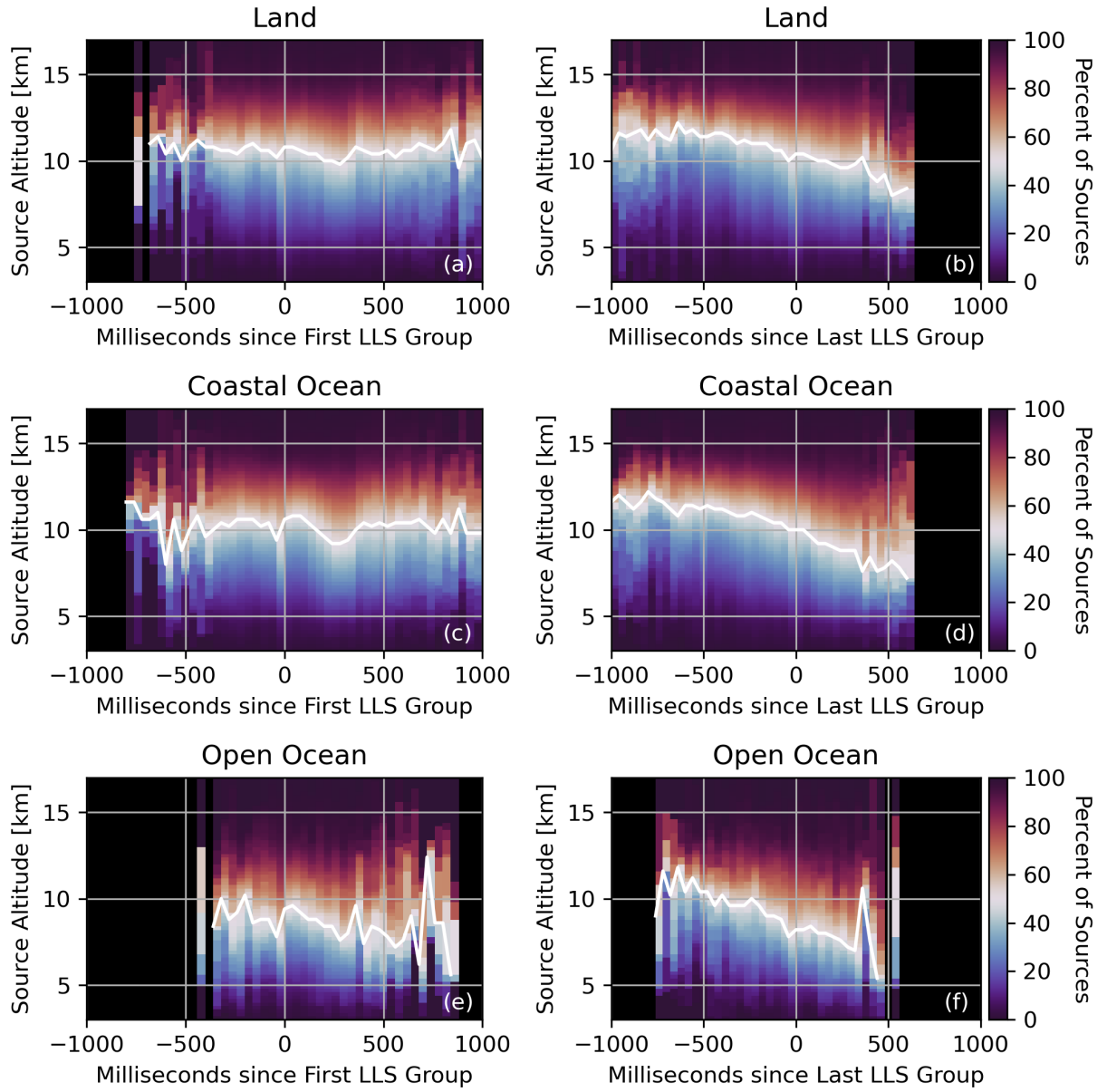
Figure 11. Cumulative distributions of source attitude at each point relative to the first LLS group in the flash (left) and the last LLS group in the flash (right). Separate distributions are shown for land (top), the coastal ocean (middle) and open ocean (bottom).
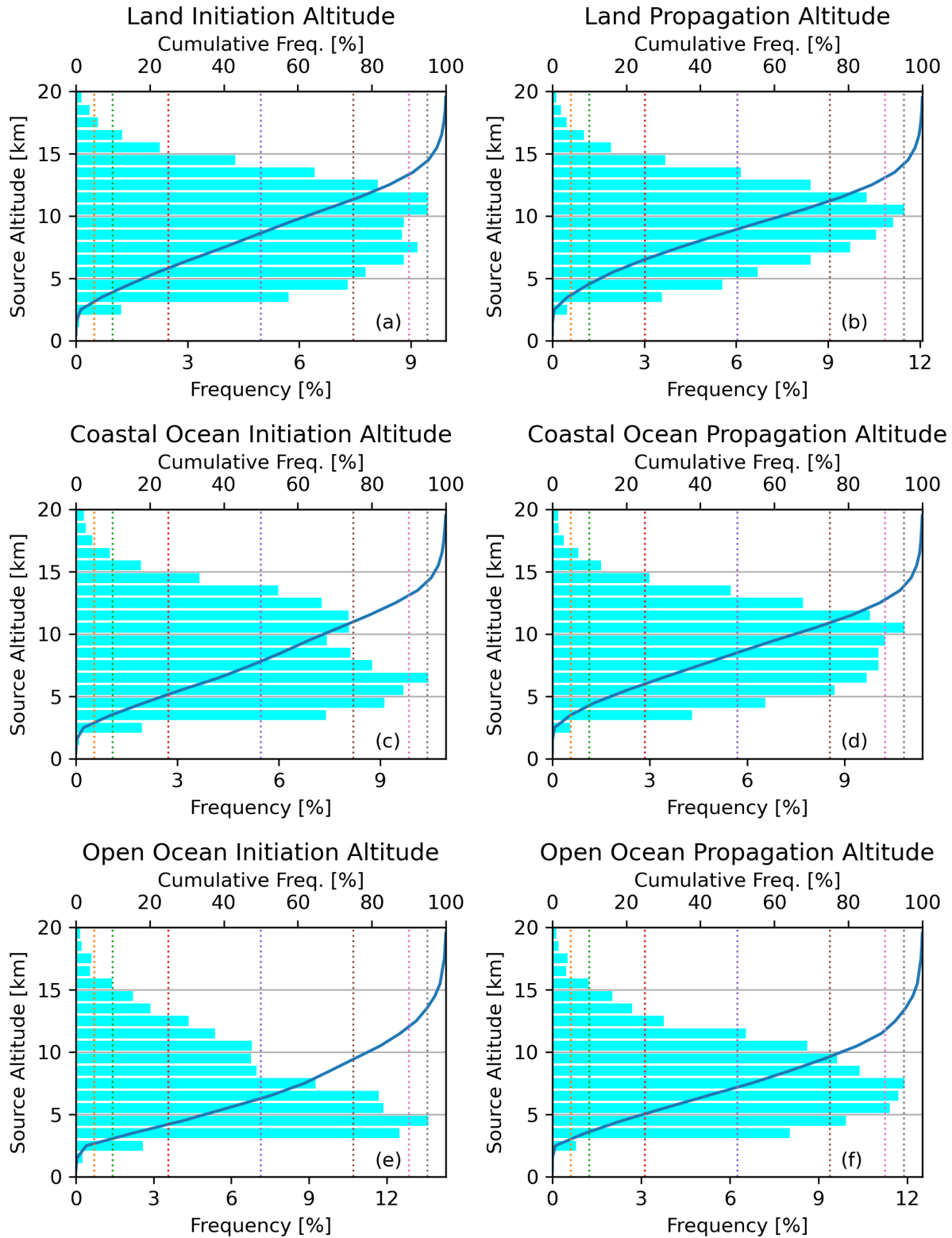
960
961 **Figure 12.** Profiles of flash initiation altitude (left column) and propagation altitude (right
962 column) for flashes over land (top row), the coastal ocean (middle row), and the open ocean
963 (bottom row).